Secondary aerosol formation in marine Arctic environments: A model measurement comparison at Ny-Ålesund

Carlton Xavier[1], Metin Baykara[1,2], Robin Wollesen de Jonge[3], Barbara Altstädter[4], Petri Clusius[1], Ville Vakkari[5,6], Roseline Thakur[1], Lisa Beck[1], Silvia Becagli[7], Mirko Severi[7], Rita Traversi[7], Radovan Krejci[8,9], Peter Tunved[8,9], Mauro Mazzola[10], Birgit Wehner[11], Mikko Sipilä[1], Markku Kulmala[1], Michael Boy[1,12], Pontus Roldin[3]

[1]Institute for Atmospheric and Earth Systems Research, University of Helsinki, P.O. Box 64, 00014 Helsinki, Finland
[2]Climate and Marine Sciences Department, Eurasia Institute of Earth Sciences, Istanbul Technical University, Maslak 34469, Istanbul, Turkey
[3]Division of Nuclear Physics, Department of Physics, Lund University, P. O. Box 118 SE-221 00 Lund, Sweden
[4]Institute of Flight Guidance, Technische Universität Braunschweig, 38108 Braunschweig, Germany
[5]Atmospheric Chemistry Research Group, Chemical Resource Beneficiation, North-West University, Potchefstroom, South Africa
[6]Finnish Meteorological Institute, POBox 503, FI-00101 Helsinki, Finland
[7]Department of Chemistry, University of Florence, Sesto Fiorentino, 50019 Florence, Italy
[8]Department of Environmental Science, Stockholm University, Stockholm, Sweden
[9]Bolin Centre for Climate Research, Stockholm University, Stockholm, Sweden
[10]National Research Council of Italy, Institute of Polar Sciences (CNR-ISP)
[11]Institute of Tropospheric Research, 04318 Leipzig, Germany
[12]LUT School of Engineering Science, Lappeenranta-Lahti University of Technology, P.O.Box 20, 53851 Lappeenranta, Finland

Correspondence: Carlton Xavier (carlton.xavier@helsinki.fi) and Pontus Roldin (pontus.roldin@nuclear.lu.se)

Abstract

In this study, we modeled the aerosol particle formation along air mass trajectories arriving at the remote Arctic research stations Gruvebadet (67 m a.s.l) and Zeppelin (474 m a.s.l), Ny-Ålesund during May 2018. The aim of this study was to improve our understanding of processes governing secondary aerosol formation in remote Arctic marine environments. We run the Lagrangian chemistry transport model ADCHEM, along air mass trajectories generated with FLEXPART v10.4. The air masses arriving at Ny-Ålesund spent most of their time over the open ice-free ocean. In order to capture the secondary aerosol formation from the DMS emitted by phytoplankton from the ocean surface, we implemented a recently developed comprehensive DMS and halogen multi-phase oxidation chemistry scheme, coupled with the widely used Master Chemical Mechanism (MCM).

The modeled median particle number size distributions are in close agreement with the observations in the marine influenced boundary layer at near sea surface Gruvebadet site. However, while the model reproduces the accumulation mode particle number concentrations

at Zeppelin, it overestimates the Aitken mode particle number concentrations by a factor of ~5.5. We attribute this to the deficiency of the model to capture the complex orographic effects on the boundary layer dynamics at Ny-Ålesund. However, the model reproduces the average vertical particle number concentration profiles within the boundary layer (0-600 m a.s.l.) above Gruvebadet, as measured with Condensation Particle Counters (CPCs) on board an Unmanned Aircraft Systems (UAS).

The model successfully reproduces the observed Hoppel minima, often seen in particle number size distributions at Ny-Ålesund. The model also supports the previous experimental findings that ion mediated H_2SO_4-NH_3 nucleation can explain the observed new particle formation in the marine Arctic boundary layer in the vicinity of Ny-Ålesund. Precursors resulting from gas and aqueous phase DMS chemistry contribute to the subsequent growth of the secondary aerosols. The growth of particles is primarily driven via H_2SO_4 condensation and formation of methane sulfonic acid (MSA) through the aqueous-phase ozonolysis of methane sulfinic acid (MSIA) in cloud and deliquescent droplets.

1. Introduction

The Earth's radiation budget is influenced both directly and indirectly by aerosols, which scatter and absorb the incoming short-wave radiation (direct effect) and serve as cloud condensation nuclei (CCN, indirect effect), affecting both short and long-wave radiation (Gantt et al., 2014; Oshima et al., 2020; Park et al., 2017; Scott et al., 2014). The Arctic environments are susceptible to perturbations in the radiation balance, with some estimates suggesting that, compared to the global average, the Arctic is warming at three times the rate, a phenomenon termed as Arctic amplification (AMAP, 2011, 2017, 2021; Lenssen et al., 2019; Tunved et al., 2013). The warming of the Arctic polar environment has accelerated sea ice loss, leading to a rapid decline in the extent and duration of snow cover and increase in permafrost thaw (AMAP, 2011, 2017; Bengtsson et al., 2013).

The Arctic aerosol number concentration shows a pronounced seasonal variation, where the late winter and early spring period is characterized by elevated accumulation mode aerosol concentrations, accompanied by trace gases (mostly anthropogenic with long-range transported trace elements such as sulfates, soot, and Peroxy Acyl Nitrates (PANs)). This annually recurring phenomenon in late winter and spring is termed the Arctic Haze (Barrie, 1986; Lupi et al., 2016; Tunved et al., 2013). This contrasts with the summer period, when the

atmospheric new particle formation is observed at Arctic sites, most likely due to low background aerosol concentrations, increased photo-chemistry and biological activity (Engvall et al., 2008; Heintzenberg et al., 2017; Tunved et al., 2013).

The climate change driven Arctic sea ice loss has a profound impact on natural aerosol production. Arrigo and van Dijken, (2015) found that decreasing and thinning of sea ice increased the rates of phytoplankton net primary production by ~20% between the years 1998 and 2009. This can lead to an increase in the emissions of primary biogenic precursors such as dimethyl sulfide (DMS), nitrogen volatiles (e.g. alkyl-amines) (Dall'Osto et al., 2017a; Dallósto et al., 2017b) and biological iodine species (Cuevas et al., 2018). DMS is emitted into the atmosphere via air-sea gas exchanges (Park et al., 2017; Uhlig et al., 2019), and accounts for ~80% of global natural sulfur emissions (Kettle and Andreae, 2000; Uhlig et al., 2019). Methane sulfonic acid (MSA) and sulphuric acid (H_2SO_4) is formed via DMS gas-phase oxidation by OH and halogen species (Cl, Br) (Hoffmann et al., 2016; Kim et al., 2021; Wollesen de Jonge et al., 2021). MSA and H_2SO_4, together with ammonia (NH_3) or amines, act as precursors contributing to new particle formation (NPF) and subsequently to CCN production, influencing cloud formation and radiative balance (Berndt et al., 2020; Dall'Osto et al., 2017b; Hoffmann et al., 2016; Kim et al., 2021, Jang et al., 2021; Park et al., 2021). NH_3 plays a major role in particle formation through stabilization of sulfuric acid clusters (Beck et al., 2021; Jokinen et al., 2018; Olenius et al., 2013). Depending on local parameters such as ocean pH, salinity and temperature, global oceans can act either as a source or sink of NH_3 (Paulot et al., 2015). Apart from participating in cluster formation, NH_3 influences the pH of marine aerosols by neutralizing the acid (H_2SO_4 and MSA) in the particles (Paulot et al., 2015). Though a few potential sources of NH_3 are known, for example coastal sea bird colonies, pockets of open water and melting sea ice in summertime Arctic, the magnitude of the emissions remain uncertain (Dall'osto et al., 2019a; Riddick et al., 2012; Wentworth et al., 2016).

DMS oxidation chemistry has been under focus, but uncertainties in climate predictions persist since the chemical transport models (CTMs) and global climate models (GCMs) employ fixed MSA and SO_2 yields from gas-phase oxidation of DMS to calculate aerosol formation (Hertel et al., 1994; Hoffmann et al., 2016; Kloster et al., 2006; Wollesen de Jonge et al., 2021). Including a detailed multi-phase (aqueous-phase chemistry coupled with gas-phase chemistry) DMS chemistry in numerical models can overcome these uncertainties (Barnes et al., 2006; Campolongo et al., 1999). Reaction intermediates such as dimethyl sulfoxide (DMSO), dimethyl sulfone ($DMSO_2$), methane sulfinic acid (MSIA) are water-

soluble, and experiments have shown that neglecting aqueous phase chemistry leads to either an under-estimation of modeled MSA (Campolongo et al., 1999), or an over-estimation of gaseous SO_2 compared to measured values (Hoffmann et al., 2016). For example, the temperature dependent ratio of MSA/non-sea-salt SO_4^{2-} (nss-SO_4^{2-}) is often used to estimate the contribution of DMS to sulfate budget (Ayers et al., 1999; Barnes et al., 2006). Campolongo et al., 1999 showed that modeling studies which included a multi-phase DMS chemistry can bridge the gap between temperature-dependent observations and modeled MSA/nss-SO_4^{2-}. Incorporating reactive halogens species over marine environments is crucial in determining the DMS oxidation pathways to either SO_2 or MSA, the aging of marine aerosols and the radiative properties of marine clouds (Hoffmann et al., 2016). Modeling studies have shown that Cl^- and BrO^- radicals in the gas phase act as important DMS sinks (Chen et al., 2018; Wollesen de Jonge et al., 2021), further underlining the role of halogen-DMS chemistry in the marine boundary layer.

Recent DMS+OH oxidation experiments performed in the AURA chamber at Aarhus University show that MSA dominates the secondary aerosol mass formation (Rosati et al., 2021). Aerosol dynamics model simulations which intended to replicate the observations during these AURA experiments, using the DMS gas-phase chemistry scheme from the Master Chemical Mechanism, MCMv3.3.1, (Jenkin et al., 1997, 2015; Saunders et al., 2003), substantially underestimates the particle mass and number concentrations and the MSA:SO_4^{2-} ratio (Rosati et al., 2021, Wollesen de Jonge, 2021). Based on these findings, Wollesen de Jonge et al. (2021) developed a new DMS multi-phase chemistry scheme based on MCM v3.3.1, CAPRAM DMS module 1.0 (DM1.0) (Hoffmann et al., 2016), a subset of the multi-phase halogen chemistry mechanism CAPRAM Halogen Module 2.0 (HM2.0) (Bräuer et al., 2013) and new reactions leading to the formation of hydroperoxymethyl thioformate (HPMTF). With the new DMS multi-phase chemistry mechanism, the aerosol dynamics model could capture the observed particle number concentrations and secondary PM MSA and SO_4^{2-} during DMS oxidation experiments performed at both dry and humid conditions at 0 ºC and 20 ºC in the AURA chamber. For more details on the DMS, halogen and multi-phase chemistry scheme used in ADCHEM, the reader is referred to the article and supplement of Wollesen de Jonge et al., (2021).

The aim of this work is to understand the processes and DMS oxidation products governing the formation and growth of the secondary aerosol in pristine remote marine Arctic region. To facilitate this, we have implemented the above mentioned DMS multi-phase chemistry mechanism into ADCHEM (see Methods section) and modeled the aerosol formation along

air mass trajectories arriving at Ny-Ålesund. We compared the model results with observations from Zeppelin (78°56' N, 11°53' E, 474 m a.s.l) and Gruvebadet (78°92' N, 11°90' E, 67 m a.s.l). These two sites represent remote marine Arctic conditions. Gruvebadet represents ground-level concentrations as it is well within the boundary layer (BL). Zeppelin on the other hand, is most often above the BL in winter months and sometimes below the BL during spring and summer months (Traversi et al., 2020). This implies that Zeppelin is more influenced by long range transport, and Gruvebadet by more local effects (Traversi et al., 2020). This, demonstrates the complexity involved in capturing the atmospheric mixing and secondary aerosol concentrations at Ny-Ålesund. The reason is that Svalbard has an orographically complex terrain comprising of mountains, glaciers, fjords and flat lands that introduce various micro-meteorological phenomena (Rader et al., 2021; Schemann and Ebell, 2020).

2. Methods

Using the combined multi-phase DMS chemistry mechanism by Wollesen de Jonge et al., (2021), MCMv3.3.1 and the monoterpene peroxy radical autoxidation mechanism (PRAM, Roldin et al., 2019; Xavier et al., 2019) we simulated aerosol particle formation within the marine boundary layer (MBL) upwind and at Ny-Ålesund between 1st - 25h May 2018, using the Aerosol Dynamics, gas and particle-phase CHEMistry and radiative transfer model ADCHEM (Öström et al., 2017; Roldin et al., 2011, 2019). We ran ADCHEM as a Lagrangian model along the air mass trajectories arriving at Zeppelin every 3 hours during the selected period (in total 200 trajectory simulations). FLEXPART v10.4 was used to calculate the air mass trajectories and potential emission sensitivity fields (Pisso et al., 2019; Stohl et al., 2005). The simulation results for the vertical distribution of newly formed aerosol (particle diameters < 12 nm) were validated against concurrent measurement data available from the ALADINA (Application of Light-Weight Aircraft for Detecting in situ Aerosol) campaign, wherein a UAS was used to investigate horizontal and vertical distribution of aerosol profiles in the marine boundary layer (ABL) (Lampert et al., 2020). Additionally, modeled particle number size distributions and PM_{10} chemical compositions were compared to the available measured particle number size distributions and PM_{10} filter samples at both Gruvebadet and Zeppelin measurement stations.

2.1 Air mass trajectories and potential emission sensitivity fields

We employed the Lagrangian particle dispersion model FLEXible PARTicle (FLEXPARTv10.4) to assess the emission sensitivities or "footprints" of air-masses origin arriving at Zeppelin during the simulation period. FLEXPART is a stochastic model used to compute dispersion of hypothetical particles, based on mean, turbulent and diffusive flows which can be run backwards in time to estimate air mass history at a site (Pisso et al., 2019). European Center for Medium-Range Weather Forecasts (ECMWF) ERA5 reanalysis meteorology with 137 height levels, 1-hour temporal and 0.5^{o} x 0.5^{o} spatial resolution, was used as an input to FLEXPART (*ERA5 hourly data on single levels from 1979 to present. Copernicus Climate Change Service (C3S) Climate Data Store (CDS). last access 30th April 2021, 10.24381/cds.adbb2d47, ERA5 hourly data on pressure levels from 1979 to present. Copernicus Climate Change Service (C3S) Climate Data Store (CDS). last access 30th April 2021, 10.24381/cds.bd0915c6*). The air-mass history was simulated 7-day backwards in time and arriving at Zeppelin (474 m a.s.l) every 3 hours (at 00:00, 03:00, 06:00, 09:00, 12:00, 15:00, 15:00 and 21:00 UTC) for the entire simulation period (1st - 25th May 2018).

FLEXPART calculated normalized emission sensitivity fields were combined with oceanic emissions (DMS, dibromomethane, tribromomethane, iodomethane), NH_3 from sea-bird colonies and anthropogenic emissions (NH_3, SO_2, CO, NO_x) derived from global inventories (see section 2.2). This was done to obtain representative emissions that consider the complete emsission source regions along the trajectories, upwind of the measurement station. Additional meteorological parameters such as temperature, pressure, sea surface temperature, specific humidity and cloud liquid water content from ERA5 reanalysis dataset were extracted along the trajectories and provided as inputs to ADCHEM.

2.2 Gas and primary particle emissions

Emissions of gas-phase biogenic volatile organic compounds (VOCs) α-pinene, β-pinene Δ3-carene, limonene, isoprene and β-caryophyllene were modeled with a 1 - dimensional version of MEGAN v2.04 (Model of Emissions of Gases and Aerosols from Nature 2.04) (Guenther et al., 2006). Gas-phase emissions of marine halogens such as tribromomethane ($CHBr_3$), dibromomethane (CH_2Br_2), iodomethane (CH_3I) were retrieved from CAMS-OCE Global oceanic emissions (CAMS-GLOB-OCE) which are available as daily means with a spatial resolution of 0.5^{o}x0.5^{o} (Granier et al., 2019; Ziska et al., 2013). CAMS-GLOB-OCE also provides gas-phase DMS emissions with the same temporal and spatial resolution (Granier et al., 2019) calculated with the air-sea flux parameterization and emission fluxes described in

(Lana et al., 2011; Nightingale et al., 2000). NH_3 emissions from seabird colonies were acquired from a global emission inventory (Riddick et al., 2012). To account for additional NH_3 fluxes from the open ocean, we used an estimated sea surface equilibrium $NH_{3(g)}$ saturation concentration of 0.5 nmol/m^3 (12.2 ppt at standard temperature and pressure (STP)) which approximately correspond to a surface ocean ammonium concentration of 0.125 mmol/m^3 (or ~3ppb, calculated based on equation 3 & 4 from Wentworth et al., 2016) at a sea surface temperature of +2 ºC. The sea surface temperature for the study period varied between -2 ºC-23ºC along the trajectories. The estimated surface ocean ammonium concentrations is in close agreement with the concentration estimated by the global ocean biogeochemical model COBALT (Stock et al., 2014) in the North Atlantic ocean, but up to a factor of ~5 higher than the concentrations simulated with other ocean biogeochemical models and/or model setups (Paulot et al., 2015). Therefore, we performed model sensitivity runs with a sea surface equilibrium $NH_{3(g)}$ concentration of 0.1 and 1 nmol/m^3. The $NH_{3(g)}$ equilibrium saturation concentrations represent the ambient surface gas-phase concentration at which the air-sea flux changes direction, with a net downward flux from air to sea if the ambient $NH_{3(g)}$ exceeds the equilibrium gas concentrations and vice versa (Wentworth et al., 2016). For the anthropogenic trace gas and primary particle emissions, we used the CAMS-GLOB-ANT v2.1 inventory, with a spatial resolution of 0.1°x0.1° (Granier et al., 2019).

In this work, we used the sea surface temperature (SST) and wind speed dependent sea-spray aerosol (SSA) emission parameterization by Sofiev et al. (2011), (further referred to as Sofiev11). Sofiev11 used a modified source function based on the parameterization of Monahan et al. (1986) and experiments by Mårtensson et al. (2003) and SEAS campaign by Clarke et al. (2006). The modified source function in Sofiev11 provides extrapolated SSA emissions between size ranges of 10 nm-10 µm, with appropriate correction functions employed for SST deviating from 298.15 K (Sofiev et al., 2011). Sofiev11 SSA parameterization shows that with increasing temperatures, emission flux for larger particles increases while the emission fluxes for smaller particles decreases (Barthel et al., 2019; Sofiev et al., 2011). We performed sensitivity tests using the temperature and wind speed dependent SSA parameterization by Salter et al., (2015), (further referred to as Salter15). Both the Salter15 and Sofiev11 are valid between 10 nm-10 µm. Model simulation comparisons between Sofiev11 and Salter15 have shown that the SSA parameterization from Sofiev11 has a stronger temperature dependence and higher particle number concentration emissions in the Aitken mode but result in lower PM_{10} emissions at temperatures below 25 ºC (Barthel et al., 2019).

2.2 ADCHEM

For this study, ADCHEM was employed as a 1 - dimensional column model with 40 logarithmically vertical layers, extending up to ~2600m. The model time step used for simulations was 30 seconds. The vertical atmospheric turbulent diffusion was solved using a modified Grisogono turbulent diffusivity scheme (Jeričević et al., 2010; Öström et al., 2017; Roldin et al., 2019). The ADCHEM aerosol module includes new particle formation, Brownian coagulation, condensation and evaporation of particles, and finally the dry and wet deposition of both particles and gases. The particle number size distributions were represented using 100 size bins ranging from 1.07 nm to 10 µm dry diameter. Clouds were assumed to be present in the model grid cells when the bulk liquid water content (LWC, extracted along the trajectory from ERA5 datasets) was greater than 0.01 g m^{-3}. As a default, we used a constant cloud supersaturation (*S)* of 0.25% and the particles were activated into cloud droplets, if the calculated water vapor supersaturation above the particle surface (S_c, calculated using Köhler theory) was smaller than *S*. For sulfate dominated aerosol particles this corresponds to a minimum dry particle activation diameter of ~80 nm (see Figure S10). During the cloud processing, each activated cloud droplet was assumed to take up an equal amount of liquid water corresponding to the total bulk LWC divided by the calculated number concentration of activated cloud droplets. The gas-liquid droplet mass transfer and dissolution of 50 species in total, including HCl, HNO_3, H_2SO_4, NH_3, HIO_3, H_2O_2, O_3, OH, BrO, NO_3, DMSO, MSIA, MSA and HPMTF and their irreversible reactions in the interstitial and activated cloud droplets are treated by the multi-phase chemistry mechanism (see Wollesen de Jonge et al. (2021) for details). The kinetic pre-processor (KPP) (Damian et al., 2002) was used to generate the multi-phase chemistry mechanism used in this study.

Recent observations of NPF at Ny-Ålesund have confirmed the importance of ion-mediated H_2SO_4-NH_3 nucleation in spring with MSA and H_2SO_4 condensation contributing to the subsequent growth of particles (Beck et al., 2021; Lee et al., 2020). In this work, the Atmosphere Cluster Dynamics Code (ACDC) (McGrath et al., 2012; Olenius et al., 2013) was coupled with ADCHEM (Roldin et al., 2019). ACDC was used to model NPF, which involved H_2SO_4 clustering with NH_3 via both neutral and ion-induced pathways with an ionization rate of 1.7 $cm^{-3}s^{-1}$. ACDC was used to solve the evolution of molecular H_2SO_4-NH_3 clusters by considering the loss of clusters by collisions, evaporation or coagulation scavenging onto larger aerosol particles. At each time step, the flux of clusters (up to ~ 5

H_2SO_4 and 5 NH_3 each) growing out of the ACDC molecule-cluster domain represents the NPF rate. These newly formed clusters are assigned to the corresponding smallest particle size bin at 1.07 nm in diameter in ADCHEM, which then simulates the condensational growth of particles and losses due to evaporation, coagulation, and wet and dry deposition.

For all simulations, we used model output from the closest height levels which can represent Gruvebadet (model height of 73.5 m a.s.l) and Zeppelin (model height of 486.0 m a.s.l).

Sensitivity Tests

Alongside the main ADCHEM simulations, *BaseCase,* we performed nine complementary scenario runs to assess the impact of different processes on the modeled aerosol concentrations. We performed simulations without aerosol in-cloud processing (*Cloudoff)*, to check the impact of in-cloud processing on the growth of aerosols. We investigated the effect of higher PM_{10} particle emissions on the chemical composition of secondary aerosols, using the sea-spray emission parameterization based on Salter et al., 2015 (*SalterSSA*). Simulations were conducted to assess the impact of lower and higher ammonia sources over the open ocean (*LowNH₃, HighNH₃*). A sensitivity test without precipitation (*NoPrecip*) was performed to test the influence of precipitation on number concentration and particle composition. Since cloud supersaturation is critical to the activation of particles and is highly uncertain, we performed two simulations with low and high cloud supersaturation (*S*=0.1%, *SSat=0.1* and *S*=0.4%, *Ssat=0.4*) to test its impact on the modelled particle distributions. This corresponds to minimum dry particle activation diameters of ~150 nm and ~60 nm respectively, for sulfate rich aerosol particles (see Figure S10). We performed a simulation without new particle formation (*NPFoff*), and finally one simulation without the dissolution and irreversible aqueous chemistry of the intermediate DMS oxidation products, SO_2 and halogens (*woDissolution*), implying that MSA, H_2SO_4 and HIO_3 is only formed in the gas-phase. Table 1. summarizes the setup for different model sensitivity test.

Table 1. Model sensitivity tests performed alongside the main *BaseCase* simulations to test the effect of different parameters on secondary aerosol formation. These sensitivity tests focus on the role of in-cloud processing and aqueous phase chemistry, the NH_3 emissions from open ocean, SSA parameterization and cloud supersaturation. The sea surface equilibrium $NH_{3(g)}$ concentrations in ppt are provided in the brackets.

Simulation	**In-cloud**	**$NH_{3(eq)}$ (nmol/m^3,**	**SSA**	**Precipitation**

	Processing	ppt)	parameterization	
BaseCase	On	0.5 (12.2)	Sofiev11	On
SalterSSA	On	0.5 (12.2)	Salter15	On
Cloudoff	On	0.5 (12.2)	Sofiev11	On
LowNH$_3$, HighNH$_3$	On	0.1 (2.4) 1.0 (24)	Sofiev11	On
NoPrecip	On	0.5 (12.2)	Sofiev11	Off
SSat0.4, SSat0.1	On	0.5 (12.2)	Sofiev11	On
NPFoff	On	0.5 (12.2)	Sofiev11	On
WoDissolution	On, but no dissolution and irreversible chemistry of intermediate DMS oxidation products	0.5 (12.2)	Sofiev11	On

2.3 Measurements

We utilized comprehensive measurements from the Ny-Ålesund Research station sites, Zeppelin observatory (Platt et al., 2022) and Gruvebadet during the period of 1st - 25th May 2018. Since 2017, the atmospheric observatory at Gruvebadet, which is located about 700 m southwest of Ny-Ålesund village at almost sea level (67 m.s.l), hosted Neutral cluster and Air Ion Spectrometer (NAIS, Manninen et al., 2010; Mirme and Mirme, 2013) for semi-permanent measurements. Here we use NAIS measured number size distribution of naturally charged (ions) in diameter size ranges between 0.8 nm-40 nm and neutral particles in the size range of 2.5 nm-42 nm, with a temporal resolution of two seconds.

During the measurement period, a scanning mobility particle sizer (SMPS), was operated to measure particle number size distribution in the diameter size range of 10 - 470 nm at Zeppelin. Concurrent SMPS data (TSI 3034, 54 channels) with diameter size ranging from 10 to 470 nm from Gruvebadet were also available (Dall'osto et al., 2019b; Moroni et al., 2020), thus, enabling us to compare the modeled particle number size distribution with the measured size distributions at both measurement stations. Daily resolution continuous aerosol samples with PM_{10} cutoff were collected at Gruvebadet using a Tecore Skypost low-volume sampler (Amore et al., 2022). The detection limit for Na^+ was 0.0001 μg m^{-3} and 0.0002 μg m^{-3} for Cl^-,

322 NH_4^+ and SO_4^{2-}. Since the field blank medians at Gruvebadet were less than 1 percentile of
323 sampled values, the field blanks were not subtracted from the sampled values (Amore et al.,
324 2022).

325 Vertical particle number concentration profiles were obtained using UAS ALADINA (Bärfuss
326 et al., 2018; Lampert et al., 2020), which was operated during the simulation period.
327 ALADINA were operated up to a height of 850 m a.s.l., thus can be used for a potential
328 closure between the two different research sites of Gruvebadet and Zeppelin. ALADINA is
329 equipped with two condensation particle counters (CPCs Model 3007, TSI Inc., St. Paul,
330 MN, USA), measuring in the size ranges of 3 nm - 2 μm (CPC1) and ~12 nm - 2 μm (CPC2)
331 (Lampert et al., 2020; Petäjä et al., 2020) . The difference between CPC1 and CPC2 provides
332 an estimate of particle number concentrations in the size of 3 - 12 nm ($N_{3\text{-}12}$), which was used
333 as an indicator of NPF. Alongside the CPCs, a host of other instruments measuring
334 meteorological parameters were operated in unison, the description of which can be found in
335 Bärfuss et al., (2018) and Lampert et al.,(2020).

336 **Evaluating temporal aspects of model performance**

337 The modeled PM_{10} inorganic chemical composition was evaluated against the measured PM_{10}
338 inorganic chemical composition using statistical estimates such as, normalized mean bias
339 (NMB), Pearson correlation coefficient (r), root mean squared error (RMSE) and fraction of
340 predictions within a factor of 2 of the observed values (FAC2). These tests were used to
341 evaluate modeled values (M_i) against observation values (O_i) at both the measurement sites.

342 Pearson correlation coefficient was calculated using the formula:

343
$$r = \frac{1}{n}\sum_{i=1}^{n}\frac{(O_i - \bar{O})}{\sigma_O}\frac{(M_i - \bar{M})}{\sigma_M} \quad \text{(Eq 1)}$$

344

345 Where σ_o and σ_M are standard deviations of the observed and modeled values, respectively.

346 Normalized mean bias (NMB) indicates if the predictions are over or underestimating the
347 observed values, with the factor representing the under or over estimation. NMB was
348 calculated using Eq. 2:

349
$$NMB = \frac{\sum_{i=1}^{n}(M_i - O_i)}{\sum_{i=1}^{n} O_i} \quad \text{(Eq 2)}$$

350

Root mean squared error (RMSE) was calculated using Eq. 3:

$$RMSE = \sqrt{\sum_{i=1}^{n} \frac{(M_i - O_i)^2}{n}} \quad \text{(Eq 3)}$$

FAC2 is a robust metric defined as the percentage of predictions which are within a factor of 2 of the observed values (Eq. 4):

$$Fac2 = 0.5 \leq \frac{M}{O} \leq 2.0 \quad \text{(Eq 4)}$$

3. Results and Discussion

In the following sections, we analyze and evaluate the model results against comprehensive measurements in Ny-Ålesund. In sub-section 3.1, we focus on the particle number size distributions at both sites, followed by gas-phase concentrations and PM_{10} inorganic chemical composition (sub-section 3.2) and the vertical nano-particle concentration profiles (sub-section 3.3). Finally, in sub-section 3.4, we analyze the results from the model sensitivity tests.

3.1 Particle number size distributions

Figure 1(a) and (b) show the observed and predicted particle number size distributions at Gruvebadet for the *BaseCase* simulation. Figure 1(a) includes SMPS observations starting from 10 to 470 nm and NAIS observations for neutral particles in the range 2.5 nm-10 nm (boundary marked by the black line) since NAIS data below 2.5 nm cannot be relied upon, owing to the presence of corona generated ions (Jayaratne et al., 2017; Manninen et al., 2011, 2016).

In the *BaseCase* simulationsthe model captures particle formation on 2nd May followed by an increasing number of Aitken and accumulation mode particles during the days of 3rd - 4th May, which is the result of more polluted air masses arriving at Ny-Ålesund from the European continent (Figure S1). Similarly, the model reproduces the particle formation on the 20th of May, specifically in the size ranges 2-8 nm, but overestimates the Aitken mode and accumulation mode particle concentration on the 21st of May. However, the model tends to underestimate the nucleation mode particle number concentrations between 10-25 nm ($N_{10\text{-}25\ nm}$) around noon, and overestimate the concentrations during the morning and evening (Figure

S2a). The model and measurements show an apparent time delay in the formation of new particles larger than 10 nm. While the measurements show a peak at 11 am the simulated $N_{10\text{-}25\ nm}$ shows a maximum at 3 am and 6 pm. The modeled $N_{10\text{-}25\ nm}$ maximum around 6 pm is likely a result of the formation of new particles around noon, which grow to >10 nm in diameter during the afternoon and evening by condensation of H_2SO_4. The predicted Aitken ($N_{25\text{-}100\ nm}$) and accumulation mode particle concentrations ($N_{>100\ nm}$) which form few days upwind of the station are overall, in good agreement with the measurements, which show a minor diurnal trend (Figure 2b-c). The measurements indicate that at Gruvebadet, $N_{10\text{-}25\ nm}$ contributes the most significant fraction of measured total number concentrations with 45.3%, while $N_{25\text{-}100\ nm}$ and $N_{100\text{-}470\ nm}$ contribute 30.5% and 23.94% respectively. However, the simulations predict greater contribution of Aitken mode (~53.85%) to total number concentration, with the $N_{10\ -\ 25\ nm}$ and $N_{100\text{-}470\ nm}$ accounting for ~ 36.58% and 9.57% respectively (Figure S2).

Figure 2 shows the measured size distribution in panel (a) and simulated size distribution in panel (b) for Zeppelin. At Zeppelin, the model overestimates the number concentration in nucleation and Aitken modes (also cf. Figure S3, supplementary). The particle number size distribution measurements at Zeppelin indicate that the relative contribution of the three modes (nucleation, Aitken and accumulation) varies to some extent when compared to Gruvebadet. Measurements show that at Zeppelin, $N_{10\text{-}25\ nm}$ contributes ~33.46%, $N_{25\text{-}100\ nm}$ 46.43% and $N_{>100\ nm}$ 20.11% to the total particle number concentrations. The model predicts lower relative contribution of $N_{10\ -\ 25\ nm}$ (26.94%), and a greater contribution of $N_{25\text{-}100\ nm}$ (63.44%) to the total simulated particle number concentrations. The diurnal trends at Zeppelin agree well with earlier measurements conducted at Zeppelin in spring by Ström et al. (2009). Additionally, the measured diurnal pattern at Zeppelin varies in comparison to Gruvebadet. At Zeppelin, the $N_{10\ -\ 25\ nm}$ concentrations peak in the afternoon and evening. The modeled

$N_{10\text{-}\ 25\ nm}$ shows only a weak diurnal trend. It should be noted that the measurements show a time delay of around 3 hours in the peak $N_{10\ -\ 25\ nm}$ concentrations at the two sites (Figure S2 and S3). This is possibly be a result of vertical mixing and dilution effects modulating the observed particle number concentrations at sites situated at different altitudes, similar to observation made at Zeppelin and Corbel by Ström et al. (2009).

ADCHEM considers the formation of new particles via both the ion-mediated and neutral H_2SO_4 -NH_3 clustering pathways. Beck et al (2021) observed dominant contribution of negatively charged H_2SO_4 -NH_3 clusters to secondary particle formation in May 2017 at Ny-

Ålesund, with HIO_3 playing a small role in the initial particle formation. However, the discrepancy in the modeled and observed diurnal trends of $N_{10\text{ - }25\text{ nm}}$ could indicate that there are other sources or vapors that might potentially contribute to the particle formation. Other possible NPF mechanism may involve amines (Olenius et al., 2013) and pure biogenic highly oxidized molecule (HOM) (neutral and ion induced) nucleation (Kirkby et al., 2016). We speculate that the exclusion of these other mechanisms (HIO_3, H_2SO_4-amines and HOM driven particle formation) might result in the discrepancies in the modeled and observed particle number concentration diurnal trends. HIO_3 induced particle formation could, e.g. play an important role if the air masses upwind of Ny-Ålesund traverse over the sea-ice covered regions (Baccarini et al., 2020; Beck et al., 2021).

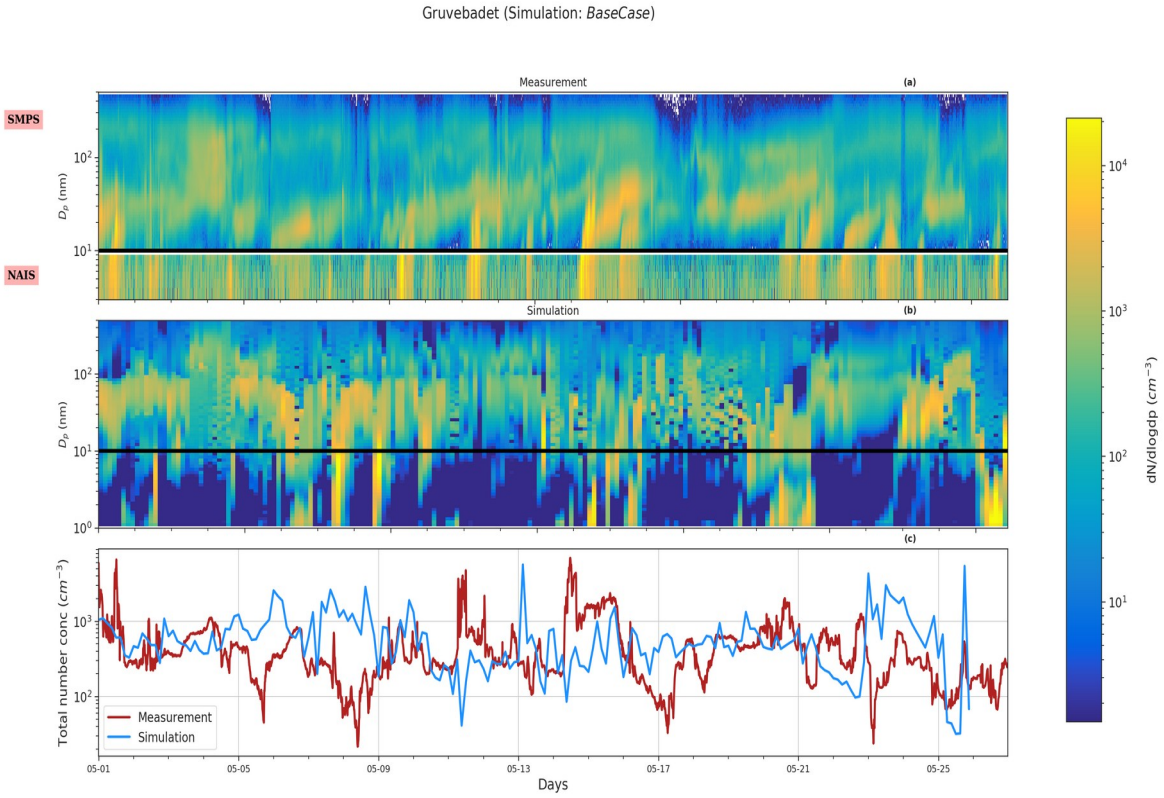

Figure 1. Particle number size distribution at Gruvebadet for *BaseCase*. The panel **(a)** shows the measurement data for the period 1-25th May from SMPS (10 nm-470 nm) and NAIS (2.5 - 10 nm), the panel **(b)** provides the modeled particle size distribution and panel **(c)** shows the total measured and simulated number concentrations. The black line at 10 nm denotes the boundary above which SMPS data starts and NAIS data ends. The abscissa indicates the time for the entire simulated duration. The ordinate in Figure 1 for both panels (a) and (b) indicates the particle diameter (D_p, nm).

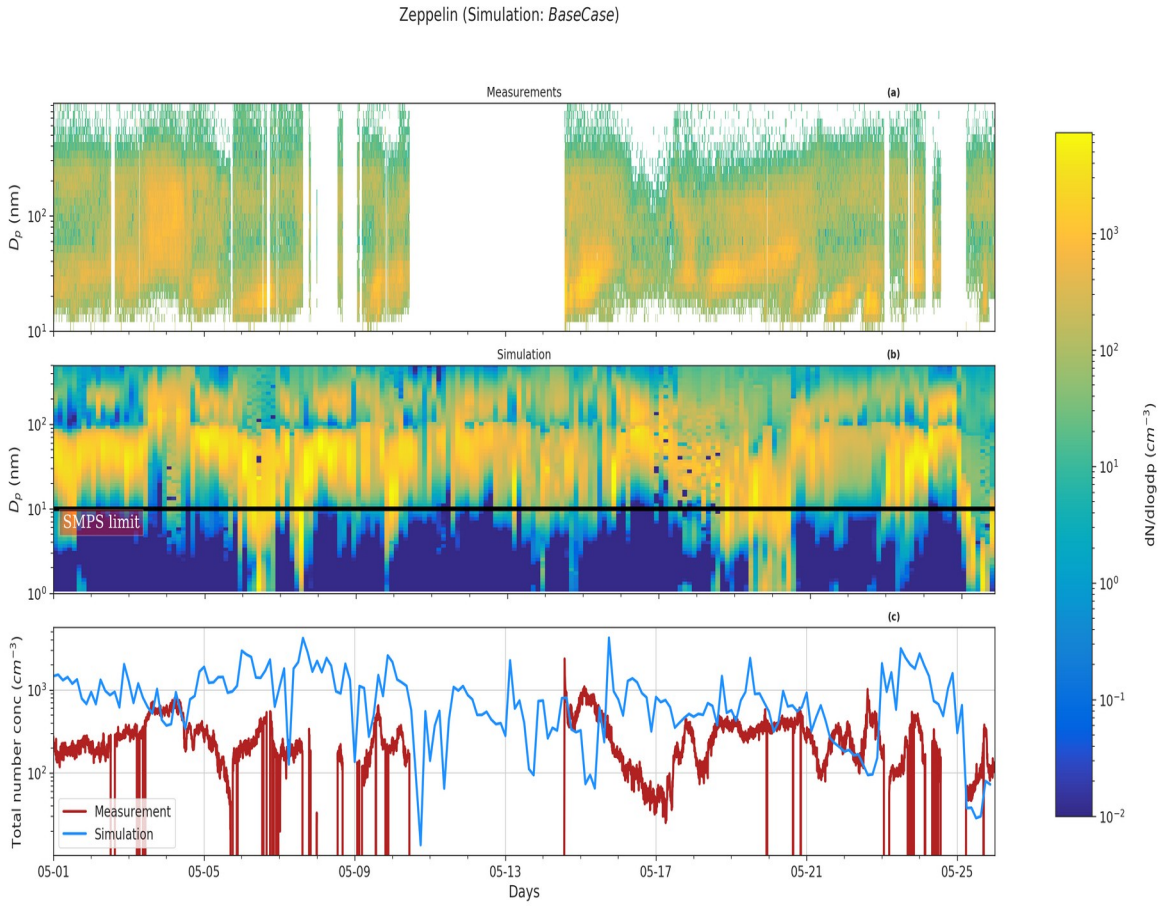

Figure 2. Particle size distribution at Zeppelin. The panel **(a)** shows the measurement data for the period 1-25th May from SMPS, the panel **(b)** provides the simulated particle size distribution and panel **(c)** shows the total measured and simulated number concentrations for the *BaseCase* simulations. The abscissa and ordinates are similar to Figure 1.

Figure 3 presents the median particle number size distribution for the *BaseCase* simulation at both Zeppelin and Gruvebadet, with respective 25th and 75th percentiles, for the entire selected period. At Gruvebadet, the modeled and measured median particle number size distributions are in reasonable agreement for both Aitken and accumulation mode. However, the model over predicts the median Aitken mode concentrations at Zeppelin by a factor ~ 5.5. The modeled Aitken mode peak at both measurement sites is ~50 nm, while the measured Aitken mode peak is ~30 nm. Though the modeled accumulation mode peak is at a larger size (~150 nm), compared to the measured accumulation mode peak (~110 nm), the predicted value is slightly lower than the monthly averaged accumulation mode peak location measured at Zeppelin in earlier studies (~160-170 nm, Dall'Osto et al., 2019).

The discrepancy between the modeled and measured particle concentrations at Zeppelin can be caused by the underlying complexity of modeling the boundary layer dynamics at an elevated site, such as Zeppelin. The vertical mixing of aerosols along the up-slope or down-slope of a mountain site is difficult, if not impossible for a 1- dimensional column model, since it is unable to capture the topographical influence on locally varying wind speeds or latent and sensible heat fluxes (Mikkola, 2020; Wainwright et al., 2012).

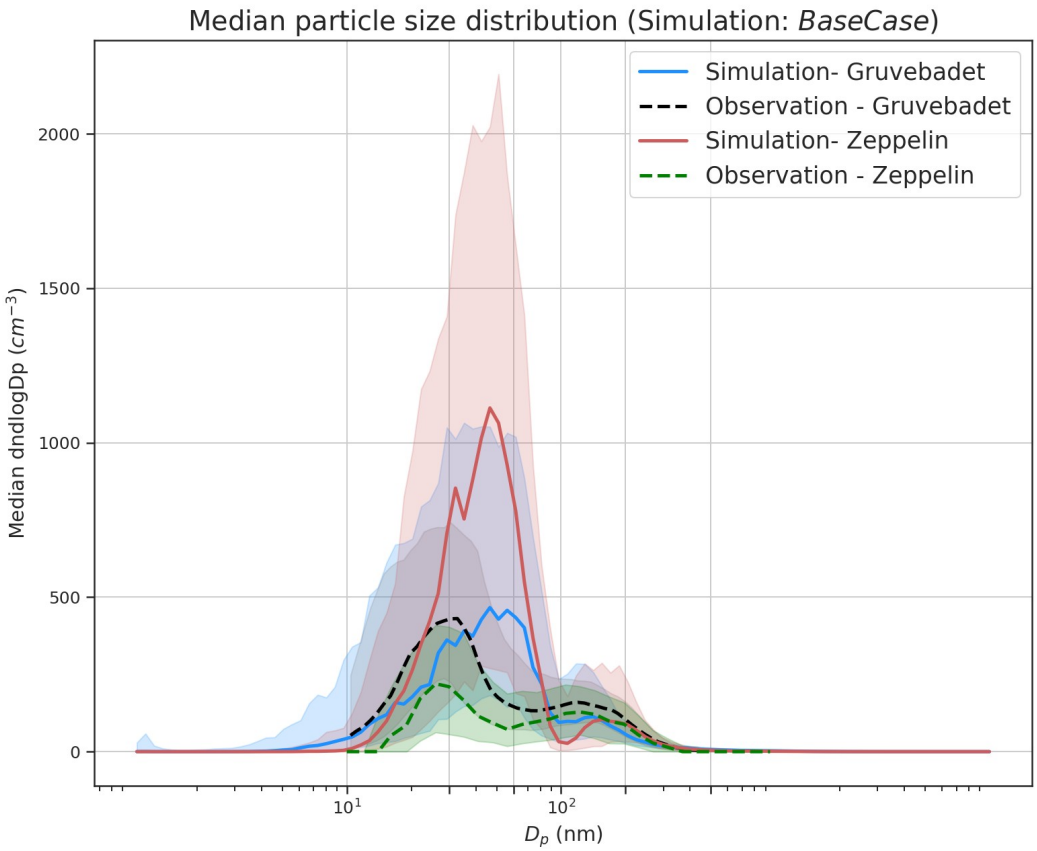

Figure 3. Median particle number size distribution at Gruvebadet and Zeppelin for both modeled (*BaseCase* simulations) and measured values. The shaded areas indicate the 25th and 75th percentiles for both model and measured median particle number size distribution. At Zeppelin, the simulated median size distribution is calculated for periods only when SMPS data were available.

Another detectable feature in the median particle number size distribution is the diameter of the Hoppel minimum (Hoppel et al., 1985, 1986), and the role of in-cloud processing in forming this minimum. A Hoppel minimum is often observed in marine air masses (Fossum

et al., 2018; Tunved et al., 2013; Zheng et al., 2018) and is attributed to in-cloud processing of aerosols, with chemical processing (e.g., sulfate production via oxidation of dissolved SO_2) (Feingold and Kreidenweis, 2000; Hoppel et al., 1986), and coalescence of droplets playing a key role (Flossmann and Wobrock, 2019; Hoppel et al., 1986; Hoppel and Frick, 1990; Noble and Hudson, 2013). It has been estimated that, on average, aerosols take part in about 10 non-precipitating cloud cycles before it is removed from the atmosphere by wet scavenging (Hoose et al., 2008; Hoppel et al., 1986; Rosenfeld et al., 2014). These non-precipitating cloud cycles facilitate the formation of hygroscopic accumulation mode particles, with low critical supersaturation (S_c) that readily activates to cloud droplets during subsequent cloud cycles, thus growing to larger sizes. This is because the activated particles undergo chemical processing, gas-to-particle conversions, coalescence and coagulation with other interstitial particles. Upon evaporation of water, the emerging dry particles have a larger size and lower S_c, leading to a minimum being formed between the un-activated and activated cloud droplets (Herenz et al., 2018; Hudson et al., 2015; Noble and Hudson, 2013). The diameter at which the Hoppel minimum is observed varies depending on the cloud supersaturation and particle composition (Hoppel et al., 1986; Hudson et al., 2015), with Hoppel minima sizes observed in ranges from 60 nm at Zeppelin Ny-Ålesund to around 90 nm at Tuktoyatuk, Canada (Herenz et al., 2018; Tunved et al., 2013).

The median particle number size distribution in Figure 3 shows that at both stations, the measured Hoppel minima is around ~ 60 nm, while the simulated Hoppel minima are around the size of ~ 100 nm at both sites. This difference in location of Hoppel minima can be attributed to the assumed value of S=0.25% in the model. The value of S used in the model lies in the range of typical marine stratocumulus clouds, which can vary between 0.1 - 1% (Fossum et al., 2018; Quinn et al., 2017). With S=0.25% the sulfate dominating particles in the Arctic marine boundary layer will be activated into cloud droplets if their diameter is greater than ~85 nm in diameter (Fig. S10).

3.2 Gas and particle-phase chemical composition of important precursors

Figure 4 shows the range of simulated gas-phase concentrations of DMS oxidation products H_2SO_4, MSA and HIO_3 for the entire period at height levels representing Gruvebadet. The mean measurement values (red dots) represent gas-phase concentrations for the same species from an earlier 2017 May campaign performed at Gruvebadet by Beck et al., (2021). Measurements of H_2SO_4 at Gruvebadet from May 2017 indicate monthly mean concentrations around ~10^6 # cm^{-3} (Beck et al., 2021). The modeled H_2SO_4 concentrations at Gruvebadet are

3 x 10^6 # cm^{-3}, implying a reasonably good model performance in predicting gaseous precursor concentrations. The simulated gas concentrations of MSA (10^5-10^8 # cm^{-3}) also agrees well with the measurements made at Gruvebadet in May 2017 by (Beck et al., 2021), wherein they measured daily averages of MSA gas concentrations in the order of 10^7 # cm^{-3}. The low modeled values of MSA and DMSO gas phase concentrations at the height representing Zeppelin (c.f. Figure S4 supplementary e.g. between 15/05 - 17/05) coincide with the period where the planetary boundary layer height (PBLH) is below the altitude of Zeppelin station (cf. Figure S5 supplementary). Overall, we can conclude that the modeled precursor gas concentrations at the two measurement sites are, in general, good agreement with earlier measurements at the two sites.

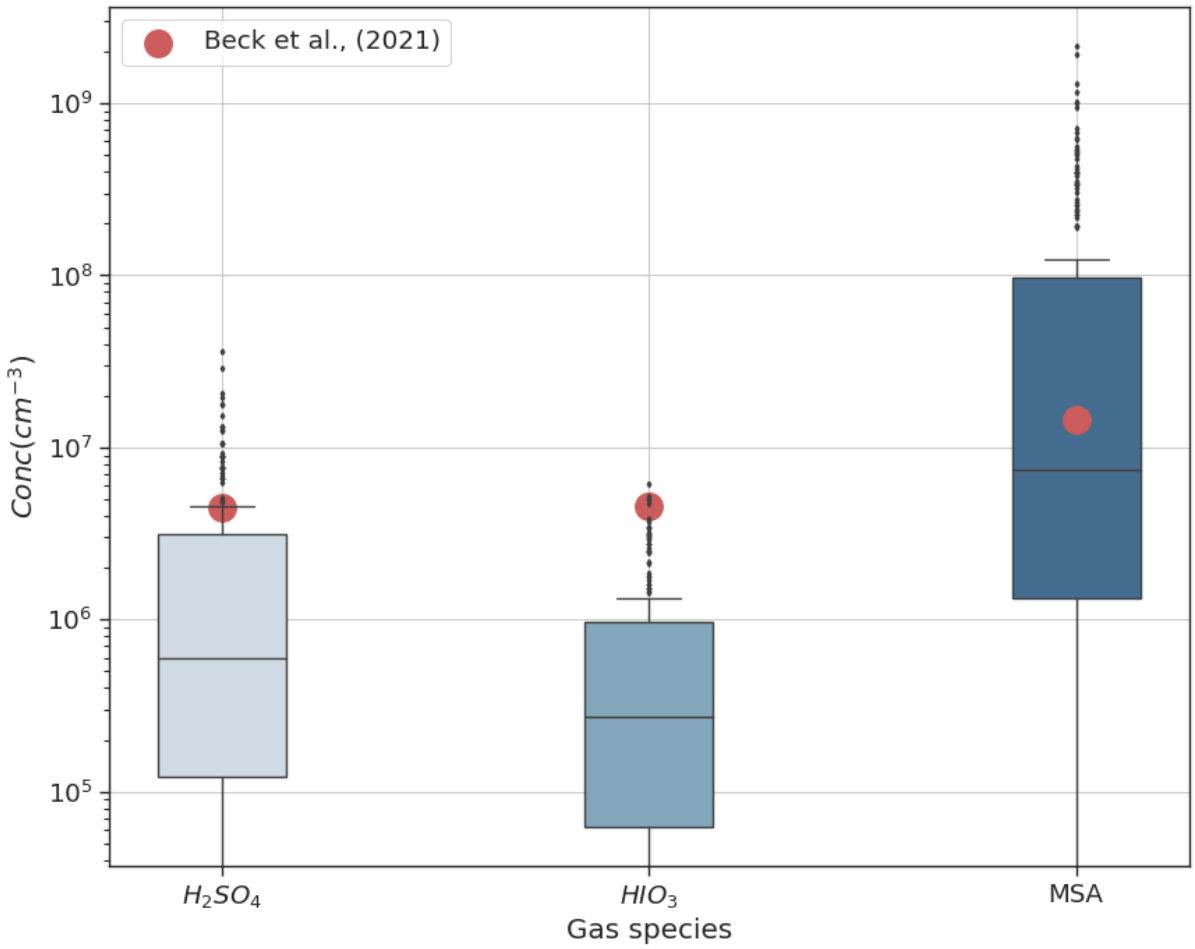

Figure 4. Gas-phase concentrations at Gruvebadet for the *BaseCase* simulations. The red dots indicate the mean measured values from an earlier 2017 May campaign conducted at Gruvebadet by Beck et al., (2021).

Figure 5 (a) shows the simulated median mass size distribution of compounds Cl^-, Na^+, MSA, SO_4^{2-}, NH_4^+, and NO_3^- for the *BaseCase* runs in the lowest model layer. Figure 5(a) indicates that the nucleation mode particles are composed mainly of SO_4^{2-} and NH_4^+, while MSA, Cl^-

and Na^+ dominate PM for larger particles. The observed and modeled high $MSA_{(g)}$ concentrations in comparison to $H_2SO_{4(g)}$ at Ny-Ålesund is not reflected in the respective vapor contribution to the nano-particle growth. This is because, in contrast to H_2SO_4, MSA is not a non-volatile condensable compound. The gas-to-particle partitioning of MSA requires co-condensation and dissolution of (NH_3) (Hodshire et al., 2019) or the existence of cations such as Na^+ which decreases the particle acidity ($[H^+]$). Figure 5(b) shows the relative mass fraction of the above-mentioned compounds to PM at different sizes. SO_4^{2-} and NH_4^+ dominate the mass for particles in the nucleation and Aitken mode. SO_4^{2-} contributes ~74% and ~71% to nucleation and Aitken mode PM, with its contribution decreasing for accumulation (100 nm-1 μm) and coarse (>1 μm) mode PM (~6% and 3.36% respectively) (Table S1). NH_4^+ contribution follows a similar trend, as SO_4^{2-}, with 12.34% and 6.95% contribution to nucleation and Aitken mode PM, but insignificant for accumulation and coarse mode PM (Table S1). The loss of primary sea spray aerosols due to wet scavenging promoted the growth of secondary aerosol particles in the nucleation and Aitken mode by NH_4^+ and SO_4^{2-} as seen in Figure 5 (b). Na^+ (~32.9%), Cl^- (~39.5%) and MSA (20.45%) are the dominant contributors to accumulation and coarse mode PM. In the *BaseCase* simulations, gas-phase SO_2 dissolves in the cloud droplets, and is oxidized by H_2O_2 into SO_4^{2-} (Wollesen de Jonge et al., 2021). Previous modeling studies have shown that a very small fraction of MSA is formed in the gas phase. Instead, most MSA is formed via ozonolysis of MSIA in the aqueous phase (Hoffmann et al., 2016; Wollesen de Jonge et al., 2021). It should be noted that HIO_3 and NO_3^- have an insignificant contribution to total PM_{10}, amounting to ~0.05% and 0.17% respectively.

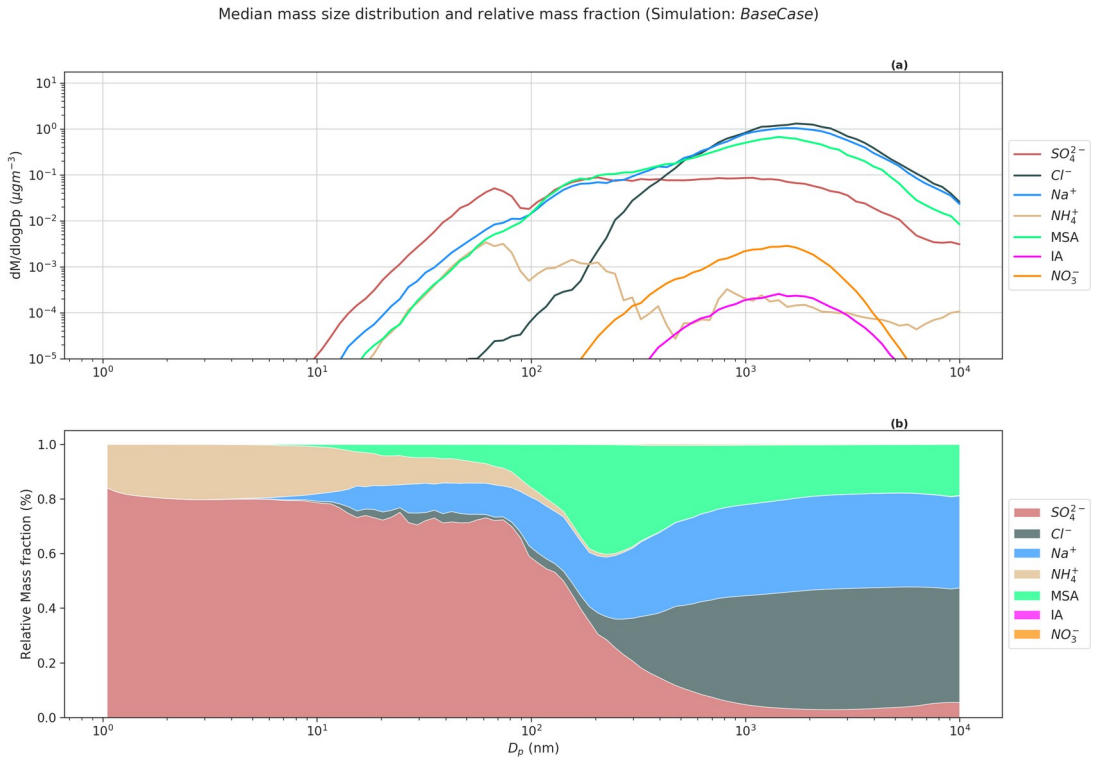

Figure 5. Simulated median mass size distribution for *BaseCase* simulations. The upper panel (a) shows the median mass size distribution for compounds Cl^-, Na^+, MSA, SO_4^{2-}, NH_4^+, HIO_3 and NO_3^- for the entire size distribution ranging from 1.07 nm-10 µm. The lower panel (b) shows the relative mass fractions or contribution of compounds Cl^-, Na^+, MSA, SO_4^{2-}, NH_4^+, HIO_3 and NO_3^- to total non-refractory PM at different sizes.

Figure 6 compares the daily PM_{10} filter measurements to the modeled values at both measurement stations. The model prediction of PM_{10} Cl^-, Na^+, SO_4^{2-} and NH_4^+, was evaluated using statistical metrics such as NMB, FAC2, correlation coefficient (*r*) and RMSE (Table 3). Though the model does well in simulating the trends of PM_{10} SO_4^{2-}, Na^+ and Cl^- at Zeppelin (*r* values of 0.35, 0.51 and 0.6 respectively), it is unable to predict the NH_4^+ trends accurately (r = -0.08).

Pearson correlation (*r* -values) at Gruvebadet are in the range of 0.29-0.34 for PM_{10} NH_4^+, SO_4^{2-}, Na^+ and Cl^- implying that the model trends are reasonably consistent with the measured trends. However, at Gruvebadet the NMB values for PM_{10} NH_4^+ and SO_4^{2-} are underpredicted (NMB = -0.88 and -0.28 respectively), while PM_{10} Na^+ and Cl^- show a large overprediction (1.81 and 1.05) in the modelled values. In contrast, at Zeppelin, the modeled PM SO_4^{2-} is overestimated (NMB=1.96). Likewise, large RMSE and negligible FAC2 values, for PM_{10} Na^+, and Cl^- imply discrepancies between the predicted and measured values, indicating that the model is overestimating PM_{10} SO_4^{2-}, Na^+ and Cl^- at Gruvebadet and PM_{10} SO_4^{2-} at

Zeppelin. In summary, the model tends to overpredict PM_{10} Na^+, Cl^- and SO_4^{2-} concentrations, but on the other hand, does reasonably well in predicting the daily measured trends. Additionally, the modeled PM_{10} Cl^-/Na^+ molar ratio at Gruvebadet and Zeppelin is ~0.79 and ~0.95, respectively. This is much higher than the observed PM_{10} Cl^-/Na^+ molar ratio at both sites (~0.39). One likely reason for this is the overestimated sea spray aerosol emissions. The PM_{10} Cl^-/Na^+ molar ratios give a measure of the acidic nature of aerosol, since increased condensation of strong acid MSA and H_2SO_4 increases acidity of aerosols thereby causing loss of Cl^- (dechlorination) as HCl (Ayers et al., 1999; Frey et al., 2020). Thus, increased availability of H_2SO_4 and MSA in particle phase in Aitken mode particles results in acid-induced Cl^- loss from sea-spray particles.

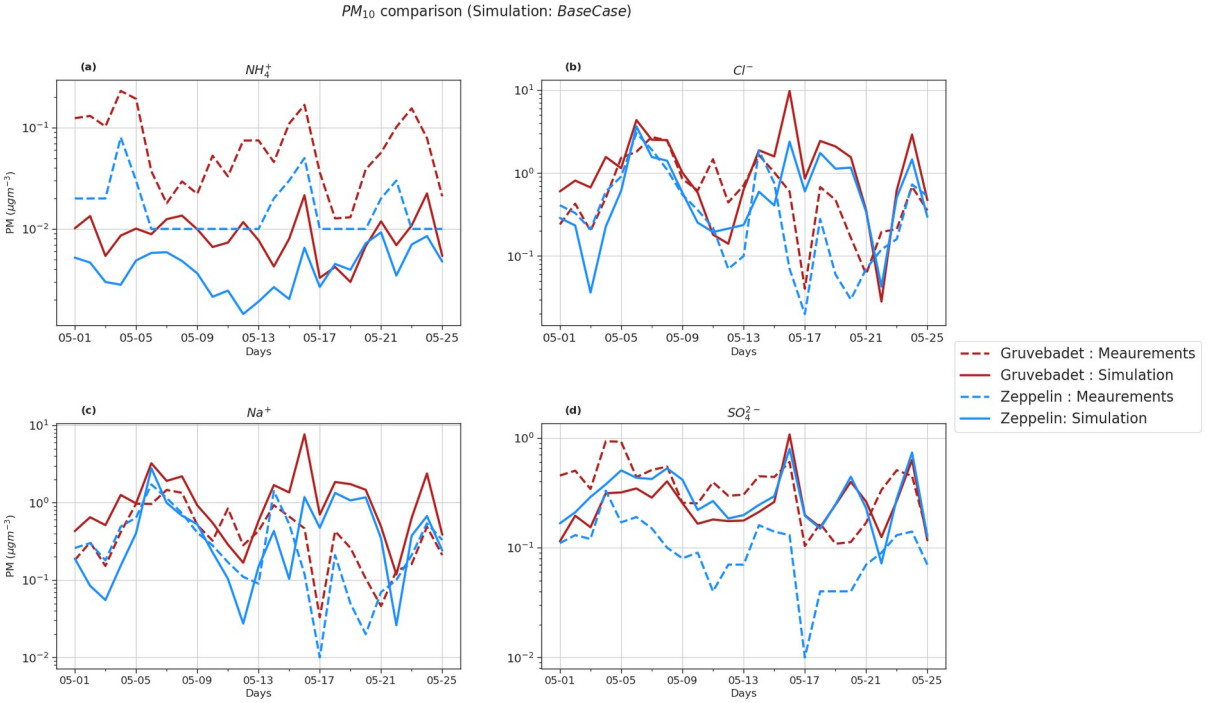

Figure 6. PM_{10} comparison of *BaseCase* simulations with daily filter samples from Gruvebadet and Zeppelin for the entire modeled period. Panel **(a)** shows PM_{10} NH_4^+, **(b)** shows PM_{10} Cl^-, **(c)** shows PM_{10} Na^+ and **(d)** shows PM_{10} SO_4^{2-} filter samples. The dotted lines in each panel indicate measurement values, and the solid line denotes simulated values. The ordinate is plotted in log scale to better visualize the low values.

Table 3: Evaluation of modeled PM_{10} values at both sites of Gruvebadet (G) and Zeppelin (Z) for the four particle-phase species Cl^-, Na^+, SO_4^{2-} and NH_4^+.

Species	Normalized mean	Correlation	RMSE (μg m^{-3})	FAC2

	bias factor (NMB)	coefficient (r)		
NH_4^+	-0.88^G , -0.76^Z	0.34^G, -0.08^Z	0.09^G, 0.02^Z	0.04^G, 0.2^Z
SO_4^{2-}	-0.28^G, 1.96^Z	0.33^G, 0.35^Z	0.27^G, 0.26^Z	0.6^G, 0.24^Z
Na^+	1.81^G, 0.36^Z	0.29^G, 0.51^Z	1.67^G, 0.55^Z	0.4^G, 0.48^Z
Cl^-	1.05^G, 0.39^Z	0.24^G, 0.60^Z	2.08^G,0.74^Z	0.24^G, 0.44^Z

570

571 **3.3 Vertical profiles of ultra-fine particle**

572 Figure 7 (a) shows the measured vertical $N_{3\text{-}12\ nm}$ concentrations from CPC onboard the UAS
573 for four measurement periods overlayed onto simulated vertical profiles. Figure 7 (b) and (c)
574 show the mean vertical profiles for $N_{3\text{-}12\ nm}$ and $N_{>12\ nm}$ for both the *BaseCase* simulation and
575 UAS measurements for the entire selected period. The model underestimates the measured $N_{3\text{-}}$
576 $_{12\ nm}$ and $N_{>12\ nm}$ vertical particle number concentrations below 200 m a.s.l. The NMB for $N_{3\text{-}12}$
577 $_{nm}$ and $N_{>12\ nm}$ is -0.28 and -0.14, respectively, implying that the model underestimates the
578 particle number concentrations. Both the modeled and measured mean particle number
579 concentrations for $N_{3\ -\ 12nm}$ and $N_{>12nm}$ are in good agreement between the heights of 200-600
580 m a.s.l. The lower calculated concentrations of modeled mean particle number concentrations
581 above 600 m a.s.l is most likely affected by higher turbulence in the transition zone from the
582 boundary layer to the free troposphere, which might cause a large mixing of aerosol particles.
583 It should be noted that, at Gruvebadet, the mean SMPS particle number concentrations are in
584 good agreement with the modeled particle number concentrations. However, at the altitude of
585 the Zeppelin station, both the model and UAS measurements of $N_{>12nm}$ are substantially
586 higher (factor of 4) than the mean particle number concentrations measured with the SMPS at
587 Zeppelin. This finding further strengthens the conclusion that the complex orography at Ny-
588 Ålesund highly affects the variability in the vertical scale, which may cause this discrepancy
589 in the observed and modeled particle number concentrations at Zeppelin (see section 3.1). The
590 UAS measurements were carried out at the airport on Ny-Ålesund (and the UAS was flown
591 around Ny-Ålesund) where the boundary layer measurements, like the model, most likely
592 resemble the general Arctic marine boundary layer conditions. Figure S9 shows the influence
593 of different sensitivity simulations on the modeled vertical particle number concentrations.
594 The large spread in the modeled vertical particle number concentrations in Figure S9,
595 highlights the importance of constraining uncertain parameters such as cloud supersaturation
596 and NH_3 gas emissions, to better simulate secondary aerosol formation in marine polar
597 regions.

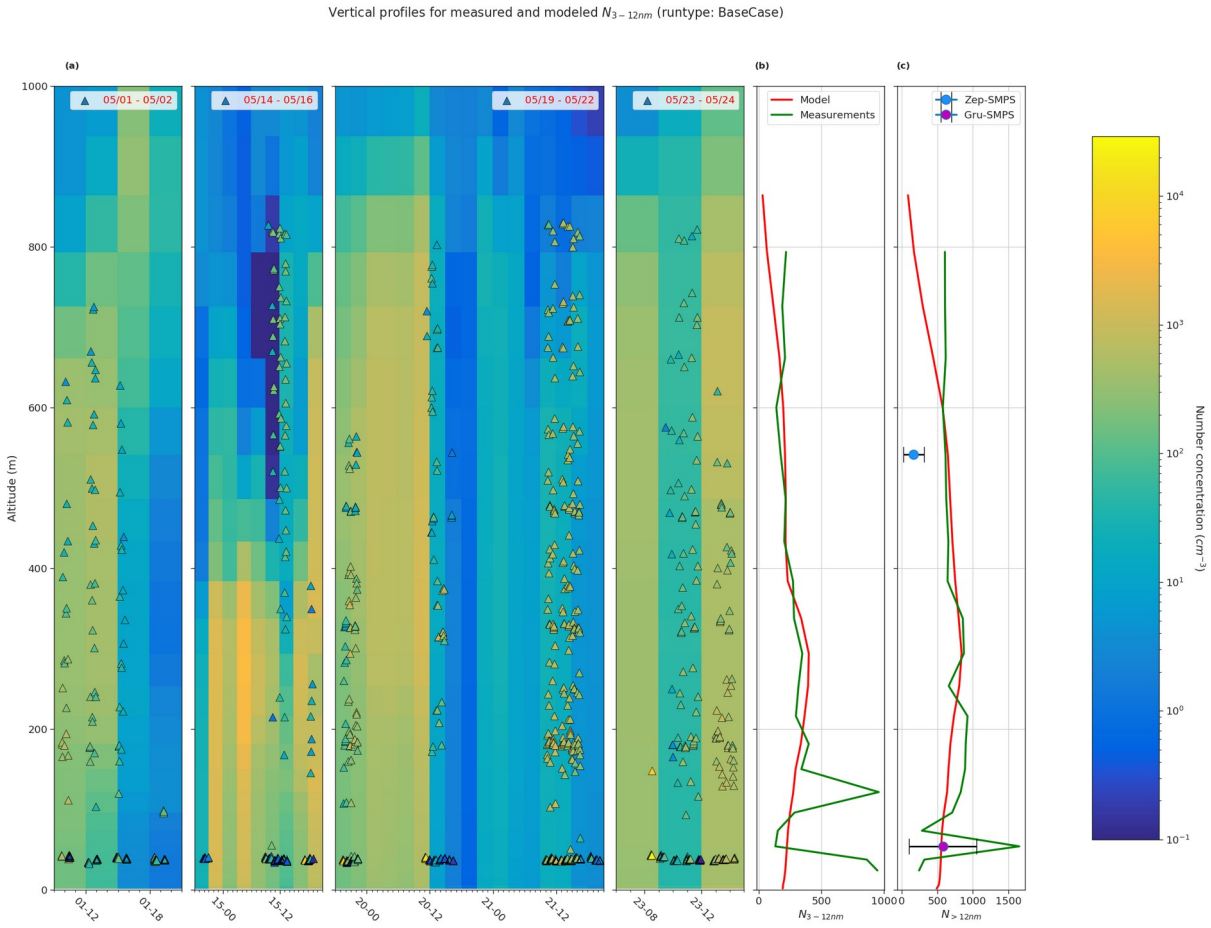

599 **Figure 7.** Comparison of vertical profiles of measured particle number concentration and
600 *BaseCase* simulation. Panel (a) shows measured particle number concentration between 3 -12
601 nm ($N_{3\text{-}12\ nm}$, triangles), from CPC onboard the UAS during 4 periods 05/01- 05/02, 05/14 -
602 05/16, 05/19- 05/22, and 05/23- 05/24 (in legend) overlayed onto the simulated $N_{3\ -\ 12nm}$ for
603 the same periods. Panel (b) shows the simulated and measured mean $N_{3\ -\ 12nm}$ and panel (c)
604 show the $N_{>12nm}$ for the selected period. Additionally, Panel (c) also shows the mean SMPS
605 particle concentrations at both Gruvebadet and Zeppelin. The horizontal bars for the mean
606 SMPS values represent the standard deviation.

607

608 **3.4 Sensitivity Tests**

609 In this section, we will discuss the results from the sensitivity tests that we performed to
610 complement the main *BaseCase* simulations. The settings of different sensitivity tests are
611 described in Table 1.

612 **Median particle size distribution for sensitivity tests**

The sensitivity study *Cloudoff* was performed to test how in-cloud processing affects the formation of larger particles, especially the accumulation mode (Figure 8). In the *Cloudoff* test, in-cloud processing was switched off in the model and the RH was set to just below supersaturation (99.9999%) in the model grid cell where clouds (RH=100.5%) exists in the *BaseCase* runs. The aim of the *Cloudoff* simulation was to investigate if the model can capture the observed accumulation mode without aerosol cloud processing. It is clear from Figure 8 (a) and (b) that in *Cloudoff* simulations, the median size distribution lacks the accumulation mode and Hoppel minima and has a higher Aitken mode particle concentration compared to either *BaseCase* or the measured median size distribution. This further emphasizes the importance of in-cloud processing in activation of particles to CCN sizes and their growth to larger sizes. However, it should be noted, that other processes such as Brownian scavenging by larger cloud droplets could result in the shift in particles from the Aitken mode to accumulation mode (as seen in median measured size distribution, Figure 8, Noble and Hudson, (2019)). Another noteworthy point in *Cloudoff* simulations is the larger number concentration of particles <10 nm compared to other cases. One plausible reason is the lack of activated cloud droplets, since the large surface areas of activated droplets are efficient at Brownian scavenging of smaller particles (Hudson et al., 2015). Likewise, the median particle number size distribution from the sensitivity tests with lower cloud supersaturation (S) of 0.1% *SSat=0.1,* reduces the accumulation mode particles, since there are fewer particles with $S_c < S$ available for activation. Increasing S to 0.4% increases accumulation mode particles, since more particles with $S_c < S$ are activated to cloud droplets (Aitken mode concentration decreases with respect to *BaseCase* simulations, since more smaller particles are activated into cloud droplets). Therefore, simulated results show that increasing the cloud supersaturation results in a higher number of smaller particles being activated into cloud droplets and shifts the simulated Hoppel minima close to the measured sizes. Figure S6, in supplementary shows median particle size distribution for all sensitivity tests.

The *SalterSSA* sensitivity test underestimates both the Aitken and accumulation mode concentrations at Gruvebadet (Figure S5, supplementary). The Salter sea-spray parameterization produces ~ 2 magnitudes fewer Aitken mode particles compared to Sofiev et. al, 2011, while the coarse mode particle emissions using *SalterSSA* parameterization are higher than Sofiev et. al 2011. This can cause MSA, H_2SO_4 and NH_3 to partition onto coarse mode particles rather than contributing to NPF and growth of the nucleation and Aitken mode particles, which substantially lowers the Aitken and accumulation mode number

647 concentrations. The *NPFoff* simulation from Figure S6 shows lower Aitken mode
648 concentrations, implying that the main contributor to Aitken mode particle number
649 concentrations are the secondary aerosols rather than the primary sea-salt particles.

650

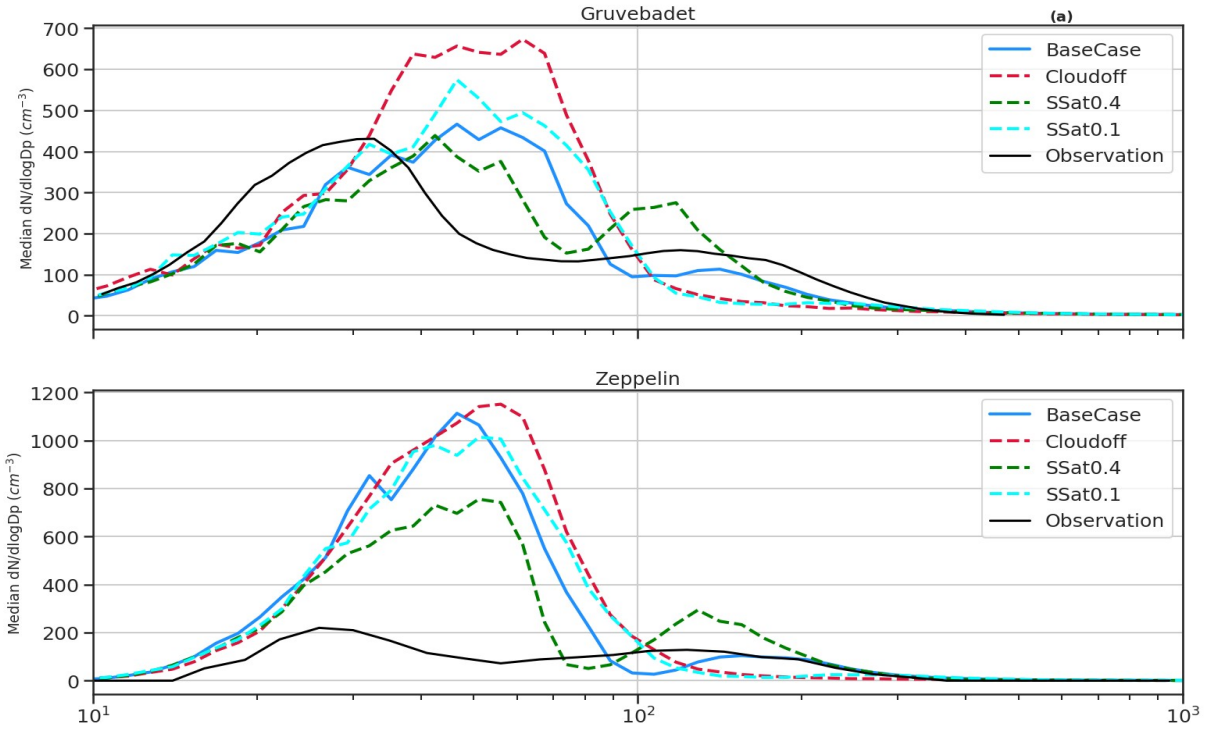

651 **Figure 8**: Median size distribution at Gruvebadet (panel (a)) and Zeppelin (panel (b)) for all
652 the sensitivity tests *Cloudoff*, *SSat=0.4*, and *SSat=0.1* (colored dashed lines) including
653 *BaseCase* (blue solid line) and observations (black solid line).

654 Another parameter of uncertainty is the concentration of NH_3 in the marine atmosphere. The
655 *LowNH₃* simulations, as expected, result in lower Aitken mode particles, whereas *HighNH₃*
656 simulations show an overprediction of Aitken mode concentrations (Figure S6,
657 supplementary). This underlines the necessity of constraining ocean and marine emissions of
658 NH_3 to better predict the aerosol particle formation in marine polar environments.

659 **Particle phase comparison for sensitivity tests**

660 Figure 9 shows the contribution of constituent compounds to PM at different particle sizes
661 with respect to the *BaseCase* simulation. The overall mean contribution of SO_4^{2-} and MSA to
662 total PM_{10} decreased by ~8% and 11% respectively, in *Cloudoff* runs compared to the
663 *BaseCase* simulations. It is expected that in non-cloud conditions there is a reduction in SO_4^{2-}
664 and MSA PM contribution because of the reduced partitioning of gaseous SO_2 to the cloud
665 droplets (for PM SO_4^{2-} formation) and inhibition of MSIA ozonolysis in the cloud droplets

(leading to PM MSA formation) (Chen et al., 2018; Hoffmann et al., 2016; Wollesen de Jonge et al., 2021). This is observed for accumulation mode particles between size ranges of 100 nm to1 μm which is characterized by lower SO_4^{2-} and MSA PM. On the other hand, PM SO_4^{2-} and MSA increase for coarse mode particles (> 1 μm). Without cloud droplet activation the deliquescent sea spray coarse mode particles become a major liquid water reservoir where MSIA and to a lesser extent SO_2 are dissolved and oxidized into MSA and SO_4^{2-}, which partly explains the increase in PM MSA and SO_4^{2-} for sizes > 1 μm. The results from *Cloudoff* simulation agrees with the findings from Wollesen de Jonge et al., 2021, who found that MSA was almost exclusively formed in the aqueous phase via MSIA ozonolysis in cloud droplets and deliquescent particles during and in between in-cloud periods. PM SO_4^{2-} in *Cloudoff* runs is mainly driven via condensation of H_2SO_4, since an increase in SO_2 gas-phase concentrations (~42% with respect to *BaseCase*) promoted gas-phase H_2SO_4 production (increase of ~44% with respect to *BaseCase*), and therefore H_2SO_4 derived PM SO_4^{2-}.

In the *woDissolution* simulation, all the PM MSA and SO_4^{2-} are a result of the condensation of $MSA_{(g)}$ and $H_2SO_{4(g)}$, since irreversible aqueous-phase chemistry is switched off. The overall contribution of PM SO_4^{2-} to the total PM_{10} increases by ~12% relative to the *BaseCase* run, while on the other hand, the contribution of PM MSA decreases by ~87% (relative to *BaseCase*). The lower PM_{10} MSA in *woDissolution* simulation emphasizes the importance of aqueous-phase formation of MSA to the growth of particles. The effect of precipitation on modeled PM (*NoPrecip*) indicates an increase in PM Na^+ and Cl^- of ~112% and 119% respectively, as compared to *BaseCase* (Figure S8). This is because of the decrease in the wet deposition of aerosol and sea-spray particles by rain events and below cloud scavenging. The consequence of neglecting precipitation results in increased condensation sink for H_2SO_4 and NH_3 (increase of 62% and 22% in PM SO_4^{2-}, NH_4^+ respectively), but since sea-spray aerosols are not scavenged by the wet removal process, the overall fractional contribution to PM by SO_4^{2-}, NH_4^+ and MSA is lower relative to *BaseCase* runs.

SalterSSA simulation results in higher PM Cl^- and Na^+ (470% and 371% increase respectively) compared to *BaseCase* runs. This is because Salter15 SSA parameterization produces larger mass emission fluxes in size ranges > 1 μm compared to Sofiev11 SSA parameterization (Barthel et al., 2019). Additionally, there is an increase of ~19% in PM MSA, largely due to formation of MSA in larger deliquescent coarse mode particles.

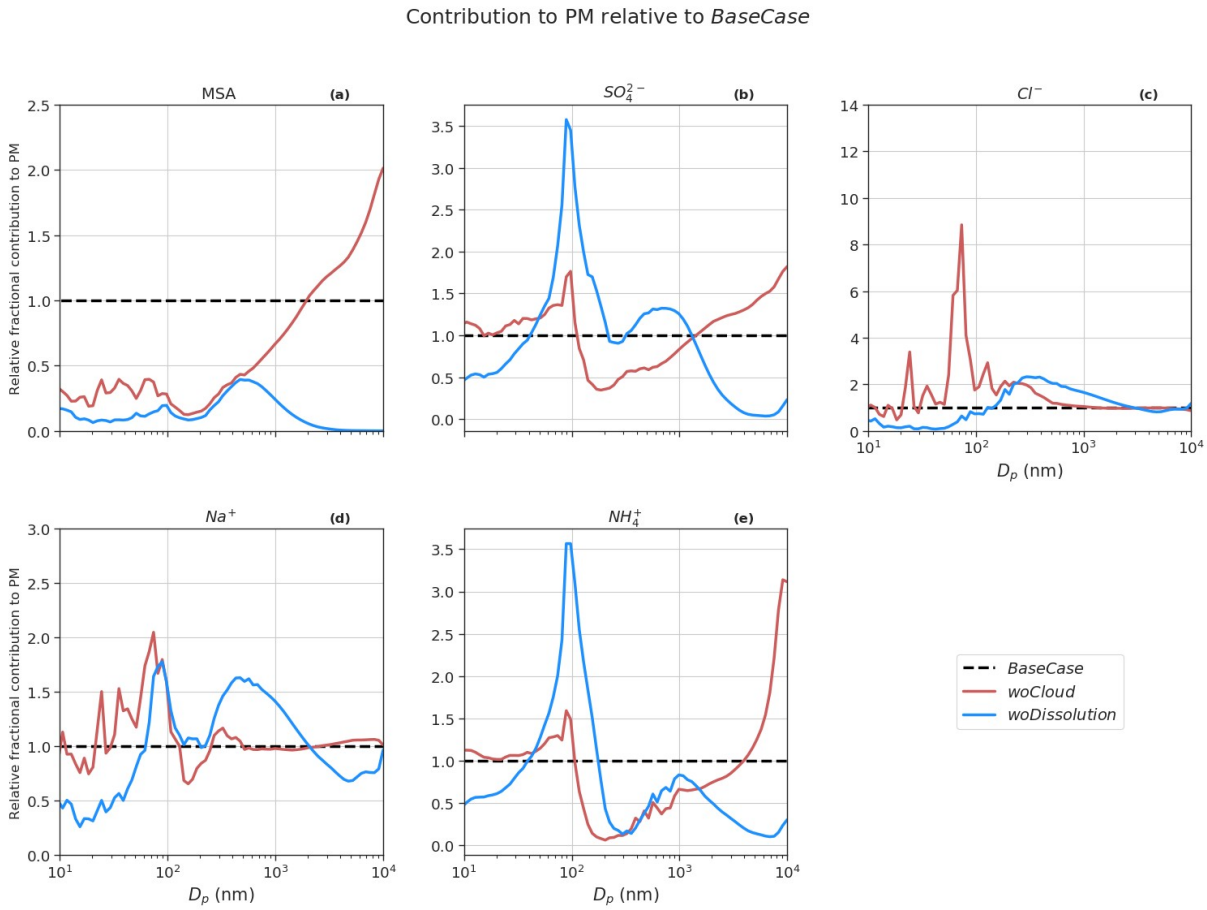

Figure 9: Contribution of constituent compounds, namely, MSA (panel (a)), SO_4^{2-} (panel (b)), Cl^- (panel(c)), Na^+ (panel (d)) and NH_4^+ (panel (e)) to PM with respect to *BaseCase* (the black dotted line).

4. Summary and conclusions

In this work, we attempt to simulate secondary aerosol formation at remote Arctic sites of Gruvebadat and Zeppelin, Ny-Ålesund, during the period of 1st - 25th of May 2018. We used the 1-dimensional column model ADCHEM which was run along FLEXPART generated Lagrangian trajectories. Since the air mass spend most of their time over the open ocean upwind of Ny-Ålesund, we use a comprehensive multi-phase DMS chemistry scheme coupled with MCMv3.3.1 and PRAM.

In the model, new particles are formed via ion-mediated H_2SO_4-NH_3 nucleation, with the initial particle growth mainly driven by condensation of H_2SO_4, while the secondary PM_{10} MSA and SO_4^{2-} contribution was mainly formed by oxidation of MSIA and SO_2 in the aqueous phase. At Gruvebadet, the modeled median particle number size distribution agrees reasonably well with the measurements, however, at Zeppelin, the simulated Aitken mode

median concentration is overestimated by a factor of 5.5. This relatively large discrepancy in modeled and measured particle size distributions at Zeppelin, and likewise the large difference between the measured particle number size distributions at Gruvebadet and Zeppelin, can to a large extent be explained by the orographic effects at Zeppelin which distorts the atmospheric boundary layer dynamics. Thus, while the model generally is able to capture the particle number size distribution dynamics in the marine boundary layer, as measured at the near sea level Gruvebadet site, it generally cannot capture the observations at the mountain station of Zeppelin, which often lies above the boundary layer and may experience free tropospheric conditions. This is also supported by the fact that $N_{>12\ nm}$ concentrations measured with the UAS above Ny-Ålesund airport agrees well with the modeled particle number concentrations, at the same altitude as Zeppelin. However, both the model and UAS $N_{>12nm}$ concentrations is a factor of 4 higher than the $N_{>12nm}$ observation at Zeppelin.

Both the measured and modeled particle size distribution, at both stations, show a distinct Hoppel minima, which can be explained by in-cloud processing. Model sensitivity runs with varying cloud supersaturation indicate that a cloud supersaturation of 0.4% or higher is required for the model to capture the observed Hoppel minima. Furthermore, model sensitivity runs show that the Aitken mode particle number concentrations are dominated by contribution of secondary aerosols rather than primary emissions. The modeled PM_{10} Cl^- and Na^+ is positively correlated when compared to PM_{10} filter samples. The main driver for secondary aerosol particle growth is the formation of MSA via aqueous phase ozonolysis of the DMS oxidation product MSIA. This demonstrates the importance of multi-phase DMS chemistry in capturing the size resolved secondary aerosol growth in marine polar regions.

The sensitivity studies indicate that it is important to limit the uncertainties in parameters such as cloud supersaturation and NH_3 emissions over open oceans to get a better constraint on secondary aerosol formation and its subsequent climatic effects. This work was a first attempt to simulate new particle and secondary aerosol formation in marine polar regions using a process based chemistry transport model that includes a comprehensive multi-phase DMS and halogen chemistry mechanism, detailed gas-molecular cluster and aerosol dynamics. In future studies, we aim to implement ADCHEM for extended studies in polar marine and remote continental regions where different atmospheric constituents such as HIO_3, terpenes and amines drive secondary aerosol formation.

Acknowledgments

The ALADINA study was funded by the German Research Foundation under grants LA 2907/5-3 and WI 1449/22-3. M. Sipilä acknowledges Academy of Finland (296628) and the European Research Council (ERC) under the European Union's Horizon 2020 research and innovation programme (GASPARCON, grant agreement no. 714621). This project has received funding from the Swedish Research Council Formas project no. 2018-01745-COBACCA, Swedish Research Council VR project no. 2019-05006, the Crafoord foundation through project number 20210969. The presented research has been also been funded by the Academy of Finland (Center of Excellence in Atmospheric Sciences) grant no. 4100200.

The authors would like to thank Tinja Olenius from the Swedish Meteorological and Hydrological (SMHI) for help with the implementation of ACDC in ADCHEM. We would also like to acknowledge the invaluable contribution of computational resources from CSC-IT Center for Science, Finland. The authors would like to thank Noora Hyytinen from the University of Oulu and University of Eastern Finland for providing the Henry's law coefficient and dissolution constants which were used in the multi-phase chemistry.

Observations at Zeppelin station were supported by Swedish Environmental Protection Agency (Naturvårdsverket) and by "Arctic Climate Across Scales (ACAS)" project funded by Knut and Alice Wallenberg Foundation and by project IWCAA funded by agency FORMAS. Authors would like to also thank for large support to Norwegian Polar Institute (NPI).

Author Contributions

CX, PR, MBoy, BA and BW planned and designed the study. PR, RWdJ and CX developed and setup the ADCHEM model. CX, MB and VV performed the FLEXPART model simulations. BA, BW, RoTh, and RT provided the measurement data. Resources were provided by PR and MBoy. CX, PR and MBoy wrote the original draft, which included visualizations made by CX and PR. All other authors discussed the results and contributed to the final manuscript.

Competing interests

The authors declare that they do have no conflict of interest.

References

AMAP: Snow, Water, Ice and Permafrost in the Arctic (SWIPA): Climate Change and the

778 Cryosphere. [online] Available from:
779 http://amap.no/swipa/%5Cnhttp://amap.no/swipa/CombinedReport.pdf%5Cnhttp://amap.no/
780 swipa/SWIPA2011ExecutiveSummaryV2.pdf%5Cnhttp://amap.no/swipa/
781 SwipaSimpleSummary-SEC.pdf, 2011.

782 AMAP: AMAP, 2017. Snow, Water, Ice and Permafrost in the Arctic (SWIPA) 2017. Arctic
783 Monitoring and Assessment Programme (AMAP), Oslo, Norway. xiv + 269 pp. [online]
784 Available from: https://www.amap.no/documents/doc/snow-water-ice-and-permafrost-in-the-
785 arctic-swipa-2017/1610, 2017.

786 AMAP: AMAP Arctic Climate Change Update 2021: Key Trends and Impacts, , 16 pp
787 [online] Available from: https://www.amap.no/documents/download/6759/inline, 2021.

788 Amore, A., Giardi, F., Becagli, S., Caiazzo, L., Mazzola, M., Severi, M. and Traversi, R.:
789 Source apportionment of sulphate in the High Arctic by a 10 yr-long record from Gruvebadet
790 Observatory (Ny-Ålesund, Svalbard Islands), Atmos. Environ., 270(July 2021),
791 doi:10.1016/j.atmosenv.2021.118890, 2022.

792 Arrigo, K. R. and van Dijken, G. L.: Continued increases in Arctic Ocean primary production,
793 Prog. Oceanogr., 136, 60–70, doi:10.1016/j.pocean.2015.05.002, 2015.

794 Ayers, G. P., Gillett, R. W., Cainey, J. M. and Dick, A. L.: Chloride and bromide loss from
795 sea-salt particles in Southern Ocean air, J. Atmos. Chem., 33(3), 299–319,
796 doi:10.1023/A:1006120205159, 1999.

797 Baccarini, A., Karlsson, L., Dommen, J., Duplessis, P., Vüllers, J., Brooks, I. M., Saiz-Lopez,
798 A., Salter, M., Tjernström, M., Baltensperger, U., Zieger, P. and Schmale, J.: Frequent new
799 particle formation over the high Arctic pack ice by enhanced iodine emissions, Nat.
800 Commun., 11(1), 1–11, doi:10.1038/s41467-020-18551-0, 2020.

801 Bärfuss, K., Pätzold, F., Altstädter, B., Kathe, E., Nowak, S., Bretschneider, L., Bestmann, U.
802 and Lampert, A.: New setup of the UAS ALADINA for measuring boundary layer properties,
803 atmospheric particles and solar radiation, Atmosphere (Basel)., 9(1),
804 doi:10.3390/atmos9010028, 2018.

805 Barnes, I., Hjorth, J. and Mihalapoulos, N.: Dimethyl sulfide and dimethyl sulfoxide and their
806 oxidation in the atmosphere, Chem. Rev., 106(3), 940–975, doi:10.1021/cr020529+, 2006.

807 Barrie, L. A.: Arctic air pollution: An overview of current knowledge, Atmos. Environ.,
808 20(4), 643–663, doi:10.1016/0004-6981(86)90180-0, 1986.

809 Barthel, S., Tegen, I. and Wolke, R.: Do new sea spray aerosol source functions improve the
810 results of a regional aerosol model?, Atmos. Environ., 198(May 2018), 265–278,
811 doi:10.1016/j.atmosenv.2018.10.016, 2019.

812 Beck, L. J., Sarnela, N., Junninen, H., Hoppe, C. J. M., Garmash, O., Bianchi, F., Riva, M.,
813 Rose, C., Peräkylä, O., Wimmer, D., Kausiala, O., Jokinen, T., Ahonen, L., Mikkilä, J.,
814 Hakala, J., He, X. C., Kontkanen, J., Wolf, K. K. E., Cappelletti, D., Mazzola, M., Traversi,
815 R., Petroselli, C., Viola, A. P., Vitale, V., Lange, R., Massling, A., Nøjgaard, J. K., Krejci, R.,

816 Karlsson, L., Zieger, P., Jang, S., Lee, K., Vakkari, V., Lampilahti, J., Thakur, R. C., Leino,
817 K., Kangasluoma, J., Duplissy, E. M., Siivola, E., Marbouti, M., Tham, Y. J., Saiz-Lopez, A.,
818 Petäjä, T., Ehn, M., Worsnop, D. R., Skov, H., Kulmala, M., Kerminen, V. M. and Sipilä, M.:
819 Differing Mechanisms of New Particle Formation at Two Arctic Sites, Geophys. Res. Lett.,
820 48(4), 1–11, doi:10.1029/2020GL091334, 2021.

821 Bengtsson, L., Hodges, K. I., Koumoutsaris, S., Zahn, M. and Berrisford, P.: The changing
822 energy balance of the polar regions in a warmer climate, J. Clim., 26(10), 3112–3129,
823 doi:10.1175/JCLI-D-12-00233.1, 2013.

824 Berndt, T., Chen, J., Møller, K. H., Hyttinen, N., Prisle, N. L., Tilgner, A., Hoffmann, E. H.,
825 Herrmann, H. and Kjaergaard, H. G.: SO2formation and peroxy radical isomerization in the
826 atmospheric reaction of OH radicals with dimethyl disulfide, Chem. Commun., 56(88),
827 13634–13637, doi:10.1039/d0cc05783e, 2020.

828 Bräuer, P., Tilgner, A., Wolke, R. and Herrmann, H.: Mechanism development and modelling
829 of tropospheric multiphase halogen chemistry: The CAPRAM Halogen Module 2.0 (HM2), J.
830 Atmos. Chem., 70(1), 19–52, doi:10.1007/s10874-013-9249-6, 2013.

831 Campolongo, F., Saltelli, A., Jensen, N. R., Wilson, J. and Hjorth, J.: The role of multiphase
832 chemistry in the oxidation of dimethylsulphide (DMS). A latitude dependent analysis, J.
833 Atmos. Chem., 32(3), 327–356, doi:10.1023/A:1006154618511, 1999.

834 Chen, Q., Sherwen, T., Evans, M. and Alexander, B.: DMS oxidation and sulfur aerosol
835 formation in the marine troposphere: A focus on reactive halogen and multiphase chemistry,
836 Atmos. Chem. Phys., 18(18), 13617–13637, doi:10.5194/acp-18-13617-2018, 2018.

837 Clarke, A. D., Owens, S. R. and Zhou, J.: An ultrafine sea-salt flux from breaking waves:
838 Implications for cloud condensation nuclei in the remote marine atmosphere, J. Geophys. Res.
839 Atmos., 111(6), doi:10.1029/2005JD006565, 2006.

840 Cuevas, C. A., Maffezzoli, N., Corella, J. P., Spolaor, A., Vallelonga, P., Kjær, H. A.,
841 Simonsen, M., Winstrup, M., Vinther, B., Horvat, C., Fernandez, R. P., Kinnison, D.,
842 Lamarque, J. F., Barbante, C. and Saiz-Lopez, A.: Rapid increase in atmospheric iodine levels
843 in the North Atlantic since the mid-20th century, Nat. Commun., 9(1), 1–6,
844 doi:10.1038/s41467-018-03756-1, 2018.

845 Dall'osto, M., Beddows, D. C. S., Tunved, P., Harrison, R. M., Lupi, A., Vitale, V., Becagli,
846 S., Traversi, R., Park, K. T., Jun Yoon, Y., Massling, A., Skov, H., Lange, R., Strom, J. and
847 Krejci, R.: Simultaneous measurements of aerosol size distributions at three sites in the
848 European high Arctic, Atmos. Chem. Phys., 19(11), 7377–7395, doi:10.5194/acp-19-7377-
849 2019, 2019a.

850 Dall'osto, M., Beddows, D. C. S., Tunved, P., Harrison, R. M., Lupi, A., Vitale, V., Becagli,
851 S., Traversi, R., Park, K. T., Jun Yoon, Y., Massling, A., Skov, H., Lange, R., Strom, J. and
852 Krejci, R.: Simultaneous measurements of aerosol size distributions at three sites in the
853 European high Arctic, Atmos. Chem. Phys., 19(11), 7377–7395, doi:10.5194/acp-19-7377-
854 2019, 2019b.

Dall'Osto, M., Ovadnevaite, J., Paglione, M., Beddows, D. C. S., Ceburnis, D., Cree, C., Cortés, P., Zamanillo, M., Nunes, S. O., Pérez, G. L., Ortega-Retuerta, E., Emelianov, M., Vaqué, D., Marrasé, C., Estrada, M., Sala, M. M., Vidal, M., Fitzsimons, M. F., Beale, R., Airs, R., Rinaldi, M., Decesari, S., Facchini, M. C., Harrison, R. M., O'Dowd, C. and Simó, R.: Antarctic sea ice region as a source of biogenic organic nitrogen in aerosols, Sci. Rep., 7(1), 1–10, doi:10.1038/s41598-017-06188-x, 2017a.

Dall'Osto, M., Beddows, D. C. S., Tunved, P., Krejci, R., Ström, J., Hansson, H. C., Yoon, Y. J., Park, K. T., Becagli, S., Udisti, R., Onasch, T., Ódowd, C. D., Simó, R. and Harrison, R. M.: Arctic sea ice melt leads to atmospheric new particle formation, Sci. Rep., 7(1), 1–10, doi:10.1038/s41598-017-03328-1, 2017b.

Damian, V., Sandu, A., Damian, M., Potra, F. and Carmichael, G. R.: The kinetic preprocessor KPP - A software environment for solving chemical kinetics, Comput. Chem. Eng., 26(11), 1567–1579, doi:10.1016/S0098-1354(02)00128-X, 2002.

Feingold, G. and Kreidenweis, S.: Does cloud processing of aerosol enhance droplet concentrations?, J. Geophys. Res. Atmos., 105(D19), 24351–24361, doi:10.1029/2000JD900369, 2000.

Flossmann, A. I. and Wobrock, W.: Cloud processing of aerosol particles in marine stratocumulus clouds, Atmosphere (Basel)., 10(9), doi:10.3390/atmos10090520, 2019.

Fossum, K. N., Ovadnevaite, J., Ceburnis, D., Dall'Osto, M., Marullo, S., Bellacicco, M., Simó, R., Liu, D., Flynn, M., Zuend, A. and O'Dowd, C.: Summertime Primary and Secondary Contributions to Southern Ocean Cloud Condensation Nuclei, Sci. Rep., 8(1), 1–14, doi:10.1038/s41598-018-32047-4, 2018.

Frey, M. M., Norris, S. J., Brooks, I. M., Anderson, P. S., Nishimura, K., Yang, X., Jones, A. E., Nerentorp Mastromonaco, M. G., Jones, D. H. and Wolff, E. W.: First direct observation of sea salt aerosol production from blowing snow above sea ice, Atmos. Chem. Phys., 20(4), 2549–2578, doi:10.5194/acp-20-2549-2020, 2020.

Gantt, B., He, J., Zhang, X., Zhang, Y. and Nenes, A.: Incorporation of advanced aerosol activation treatments into CESM/CAM5: Model evaluation and impacts on aerosol indirect effects, Atmos. Chem. Phys., 14(14), 7485–7497, doi:10.5194/acp-14-7485-2014, 2014.

Granier, C., Darras, S., Gon, H. D. van der, Jana, D., Elguindi, N., Bo, G., Michael, G., Marc, G., Jalkanen, J.-P., Kuenen, J., Liousse, C., Quack, B., Simpson, D. and Sindelarova, K.: The Copernicus Atmosphere Monitoring Service global and regional emissions (April 2019 version), , (April) [online] Available from: https://hal.archives-ouvertes.fr/hal-02322431%0Ahttps://hal.archives-ouvertes.fr/hal-02322431/document, 2019.

Guenther, A., Karl, T., Harley, P., Weidinmyer, C., Palmer, P. I. and Geron, C.: Edinburgh Research Explorer Estimates of global terrestrial isoprene emissions using MEGAN (Model of Emissions of Gases and Aerosols from Nature) and Physics Estimates of global terrestrial isoprene emissions using MEGAN (Model of Emissions of Gases an, Atmos. Chem. Phys., (6), 3181–3210, 2006.

894 Herenz, P., Wex, H., Henning, S., Kristensen, T. B., Rubach, F., Roth, A., Borrmann, S.,
895 Bozem, H., Schulz, H. and Stratmann, F.: Measurements of aerosol and CCN properties in the
896 Mackenzie River delta (Canadian Arctic) during spring--summer transition in May 2014,
897 Atmos. Chem. Phys., 18(7), 4477–4496, doi:10.5194/acp-18-4477-2018, 2018.

898 Hertel, O., Christensen, J. and Hov, Ø.: Modelling of the end products of the chemical
899 decomposition of DMS in the marine boundary layer, Atmos. Environ., 28(15), 2431–2449,
900 doi:10.1016/1352-2310(94)90395-6, 1994.

901 Hodshire, A. L., Campuzano-Jost, P., Kodros, J. K., Croft, B., Nault, B. A., Schroder, J. C.,
902 Jimenez, J. L. and Pierce, J. R.: The potential role of methanesulfonic acid (MSA) in aerosol
903 formation and growth and the associated radiative forcings, Atmos. Chem. Phys., 19(5),
904 3137–3160, doi:10.5194/acp-19-3137-2019, 2019.

905 Hoffmann, E. H., Tilgner, A., Schrödner, R., Bräuer, P., Wolke, R. and Herrmann, H.: An
906 advanced modeling study on the impacts and atmospheric implications of multiphase
907 dimethyl sulfide chemistry, Proc. Natl. Acad. Sci. U. S. A., 113(42), 11776–11781,
908 doi:10.1073/pnas.1606320113, 2016.

909 Hoose, C., Lohmann, U., Bennartz, R., Croft, B. and Lesins, G.: Global simulations of aerosol
910 processing in clouds, Atmos. Chem. Phys., 8(23), 6939–6963, doi:10.5194/acp-8-6939-2008,
911 2008.

912 Hoppel, W. A. and Frick, G. M.: Submicron aerosol size distributions measured over the
913 tropical and South Pacific, Atmos. Environ. Part A, Gen. Top., 24(3), 645–659,
914 doi:10.1016/0960-1686(90)90020-N, 1990.

915 Hoppel, W. A., Fitzgerald, J. W. and Larson, R. E.: Aerosol size distributions in air masses
916 advecting off the east coast of the United States., J. Geophys. Res., 90(D1), 2365–2379,
917 doi:10.1029/JD090iD01p02365, 1985.

918 Hoppel, W. A., Frick, G. M. and Larson, R. E.: Effect of nonprecipitating clouds on the
919 aerosol size distribution in the marine boundary layer, Geophys. Res. Lett., 13, 125–128,
920 1986.

921 Hudson, J. G., Noble, S. and Tabor, S.: Cloud supersaturations from CCN spectra Hoppel
922 minima, J. Geophys. Res., 120(8), 3436–3452, doi:10.1002/2014JD022669, 2015.

923 Jang, S., Park, K. T., Lee, K., Yoon, Y. J., Kim, K., Chung, H. Y., Jang, E., Becagli, S., Lee,
924 B. Y., Traversi, R., Eleftheriadis, K., Krejci, R. and Hermansen, O.: Large seasonal and
925 interannual variations of biogenic sulfur compounds in the Arctic atmosphere (Svalbard;
926 78.9g N, 11.9g E), Atmos. Chem. Phys., 21(12), 9761–9777, doi:10.5194/acp-21-9761-2021,
927 2021.

928 Jenkin, M. E., Saunders, S. M. and Pilling, M. J.: The tropospheric degradation of volatile
929 organic compounds: A protocol for mechanism development, Atmos. Environ., 31(1), 81–
930 104, doi:10.1016/S1352-2310(96)00105-7, 1997.

931 Jenkin, M. E., Young, J. C. and Rickard, A. R.: The MCM v3.3.1 degradation scheme for

isoprene, Atmos. Chem. Phys., 15(20), 11433–11459, doi:10.5194/acp-15-11433-2015, 2015.

Jeričević, A., Kraljević, L., Grisogono, B., Fagerli, H. and Večenaj, Ž.: Parameterization of vertical diffusion and the atmospheric boundary layer height determination in the EMEP model, Atmos. Chem. Phys., 10(2), 341–364, doi:10.5194/acp-10-341-2010, 2010.

Jokinen, T., Sipilä, M., Kontkanen, J., Vakkari, V., Tisler, P., Duplissy, E. M., Junninen, H., Kangasluoma, J., Manninen, H. E., Petäjä, T., Kulmala, M., Worsnop, D. R., Kirkby, J., Virkkula, A. and Kerminen, V. M.: Ion-induced sulfuric acid–ammonia nucleation drives particle formation in coastal Antarctica, Sci. Adv., 4(11), 1–7, doi:10.1126/sciadv.aat9744, 2018.

Kettle, A. J. and Andreae, M. O.: Flux of dimethylsulfide from the oceans: A comparison of updated data sets and flux models, J. Geophys. Res. Atmos., 105(D22), 26793–26808, doi:10.1029/2000JD900252, 2000.

Kim, I., Zhang, M., Kim, K. and Park, K.: First high-frequency underway observation of dms distribution in the southern ocean during austral autumn, Atmosphere (Basel)., 12(1), 1–10, doi:10.3390/atmos12010122, 2021.

Kirkby, J., Duplissy, J., Sengupta, K., Frege, C., Gordon, H., Williamson, C., Heinritzi, M., Simon, M., Yan, C., Almeida, J., Trostl, J., Nieminen, T., Ortega, I. K., Wagner, R., Adamov, A., Amorim, A., Bernhammer, A. K., Bianchi, F., Breitenlechner, M., Brilke, S., Chen, X., Craven, J., Dias, A., Ehrhart, S., Flagan, R. C., Franchin, A., Fuchs, C., Guida, R., Hakala, J., Hoyle, C. R., Jokinen, T., Junninen, H., Kangasluoma, J., Kim, J., Krapf, M., Kurten, A., Laaksonen, A., Lehtipalo, K., Makhmutov, V., Mathot, S., Molteni, U., Onnela, A., Perakyla, O., Piel, F., Petaja, T., Praplan, A. P., Pringle, K., Rap, A., Richards, N. A. D., Riipinen, I., Rissanen, M. P., Rondo, L., Sarnela, N., Schobesberger, S., Scott, C. E., Seinfeld, J. H., Sipila, M., Steiner, G., Stozhkov, Y., Stratmann, F., Tomé, A., Virtanen, A., Vogel, A. L., Wagner, A. C., Wagner, P. E., Weingartner, E., Wimmer, D., Winkler, P. M., Ye, P., Zhang, X., Hansel, A., Dommen, J., Donahue, N. M., Worsnop, D. R., Baltensperger, U., Kulmala, M., Carslaw, K. S. and Curtius, J.: Ion-induced nucleation of pure biogenic particles, Nature, 533(7604), 521–526, doi:10.1038/nature17953, 2016.

Kloster, S., Feichter, J., Maier-Reimer, E., Six, K. D., Stier, P. and Wetzel, P.: DMS cycle in the marine ocean-atmosphere system - A global model study, Biogeosciences, 3(1), 29–51, doi:10.5194/bg-3-29-2006, 2006.

Lampert, A., Altstädter, B., Bärfuss, K., Bretschneider, L., Sandgaard, J., Michaelis, J., Lobitz, L., Asmussen, M., Damm, E., Käthner, R., Krüger, T., Lüpkes, C., Nowak, S., Peuker, A., Rausch, T., Reiser, F., Scholtz, A., Sotomayor-Zakharov, D., Gaus, D., Bansmer, S., Wehner, B. and Pätzold, F.: Unmanned aerial systems for investigating the polar atmospheric boundary layer-technical challenges and examples of applications, Atmosphere (Basel)., 11(4), doi:10.3390/ATMOS11040416, 2020.

Lana, A., Bell, T. G., Simó, R., Vallina, S. M., Ballabrera-Poy, J., Kettle, A. J., Dachs, J., Bopp, L., Saltzman, E. S., Stefels, J., Johnson, J. E. and Liss, P. S.: An updated climatology

971 of surface dimethlysulfide concentrations and emission fluxes in the global ocean, Global
972 Biogeochem. Cycles, 25(1), 1–17, doi:10.1029/2010GB003850, 2011.

973 Lee, H., Lee, K., Lunder, C. R., Krejci, R., Aas, W., Park, J., Park, K.-T., Lee, B. Y., Yoon,
974 Y. J. and Park, K.: Atmospheric new particle formation characteristics in the Arctic as
975 measured at Mount Zeppelin, Svalbard, from 2016 to 2018, Atmos. Chem. Phys., 20(21),
976 13425–13441, doi:10.5194/acp-20-13425-2020, 2020..

977 Lenssen, N. J. L., Schmidt, G. A., Hansen, J. E., Menne, M. J., Persin, A., Ruedy, R. and
978 Zyss, D.: Improvements in the GISTEMP Uncertainty Model, J. Geophys. Res. Atmos.,
979 124(12), 6307–6326, doi:10.1029/2018JD029522, 2019.

980 Lupi, A., Busetto, M., Becagli, S., Giardi, F., Lanconelli, C., Mazzola, M., Udisti, R.,
981 Hansson, H. C., Henning, T., Petkov, B., Ström, J., Krejci, R., Tunved, P., Viola, A. Pietro
982 and Vitale, V.: Multi-seasonal ultrafine aerosol particle number concentration measurements
983 at the Gruvebadet observatory, Ny-Ålesund, Svalbard Islands, Rend. Lincei, 27, 59–71,
984 doi:10.1007/s12210-016-0532-8, 2016.

985 Mårtensson, E. M., Nilsson, E. D., de Leeuw, G., Cohen, L. H. and Hansson, H.-C.:
986 Laboratory simulations and parameterization of the primary marine aerosol production, J.
987 Geophys. Res. Atmos., 108(D9), doi:https://doi.org/10.1029/2002JD002263, 2003.

988 Mikkola, J.: Slope and valley winds in the Himalayas as simulated by the Weather Research
989 and Forecasting model, , 42, 2020.

990 Monahan, E. C., Spiel, D. E. and Davidson, K. L.: A Model of Marine Aerosol Generation
991 Via Whitecaps and Wave Disruption, in Oceanic Whitecaps: And Their Role in Air-Sea
992 Exchange Processes, edited by E. C. Monahan and G. Mac Niocaill, pp. 167–174, Springer
993 Netherlands, Dordrecht., 1986.

994 Moroni, B., Ritter, C., Crocchianti, S., Markowicz, K., Mazzola, M., Becagli, S., Traversi, R.,
995 Krejci, R., Tunved, P. and Cappelletti, D.: Individual Particle Characteristics, Optical
996 Properties and Evolution of an Extreme Long-Range Transported Biomass Burning Event in
997 the European Arctic (Ny-Ålesund, Svalbard Islands), J. Geophys. Res. Atmos., 125(5), 1–17,
998 doi:10.1029/2019JD031535, 2020.

999 Nightingale, P. D., Liss, P. S. and Schlosser, P.: Measurements of air-sea gas transfer during
1000 an open ocean algal bloom, Geophys. Res. Lett., 27(14), 2117–2120,
1001 doi:10.1029/2000GL011541, 2000.

1002 Noble, S. and Hudson, J. G.: Cloud supersaturations and Hoppel minima, AIP Conf. Proc.,
1003 1527(September), 706–709, doi:10.1063/1.4803368, 2013.

1004 Noble, S. R. and Hudson, J. G.: Effects of Continental Clouds on Surface Aitken and
1005 Accumulation Modes, J. Geophys. Res. Atmos., 124(10), 5479–5502,
1006 doi:10.1029/2019JD030297, 2019.

1007 Olenius, T., Kupiainen-Määttä, O., Ortega, I. K., Kurtén, T. and Vehkamäki, H.: Free energy
1008 barrier in the growth of sulfuric acid-ammonia and sulfuric acid-dimethylamine clusters, J.

Chem. Phys., 139(8), doi:10.1063/1.4819024, 2013.

Oshima, N., Yukimoto, S., Deushi, M., Koshiro, T., Kawai, H., Tanaka, T. Y. and Yoshida, K.: Global and Arctic effective radiative forcing of anthropogenic gases and aerosols in MRI-ESM2.0, Prog. Earth Planet. Sci., 7(1), doi:10.1186/s40645-020-00348-w, 2020.

Öström, E., Putian, Z., Schurgers, G., Mishurov, M., Kivekäs, N., Lihavainen, H., Ehn, M., Rissanen, M. P., Kurtén, T., Boy, M., Swietlicki, E. and Roldin, P.: Modeling the role of highly oxidized multifunctional organic molecules for the growth of new particles over the boreal forest region, Atmos. Chem. Phys., 17(14), 8887–8901, doi:10.5194/acp-17-8887-2017, 2017.

Park, K. T., Jang, S., Lee, K., Yoon, Y. J., Kim, M. S., Park, K., Cho, H. J., Kang, J. H., Udisti, R., Lee, B. Y. and Shin, K. H.: Observational evidence for the formation of DMS-derived aerosols during Arctic phytoplankton blooms, Atmos. Chem. Phys., 17(15), 9665–9675, doi:10.5194/acp-17-9665-2017, 2017.

Park, K. T., Yoon, Y. J., Lee, K., Tunved, P., Krejci, R., Ström, J., Jang, E., Kang, H. J., Jang, S., Park, J., Lee, B. Y., Traversi, R., Becagli, S. and Hermansen, O.: Dimethyl Sulfide-Induced Increase in Cloud Condensation Nuclei in the Arctic Atmosphere, Global Biogeochem. Cycles, 35(7), 1–15, doi:10.1029/2021GB006969, 2021.

Paulot, F., Jacob, D. J., Johnson, M. T., Bell, T. G., Baker, A. R., Keene, W. C., Lima, I. D., Doney, S. C. and Stock, C. A.: Global oceanic emission of ammonia: Constraints from seawater and atmospheric observations, Global Biogeochem. Cycles, 29(8), 1165–1178, doi:10.1002/2015GB005106, 2015.

Petäjä, T., Duplissy, E., Tabakova, K., Schmale, J., Altstädter, B. and Ancellet, G.: Overview : Integrative and Comprehensive Understanding on Polar Environments (iCUPE) – concept and initial results, , 8551–8592, 2020.

Pisso, I., Sollum, E., Grythe, H., Kristiansen, N., Cassiani, M., Eckhardt, S., Arnold, D., Morton, D., Thompson, R., Groot Zwaaftink, C., Evangeliou, N., Sodemann, H., Haimberger, L., Henne, S., Brunner, D., Burkhart, J., Fouilloux, A., Brioude, J., Philipp, A., Seibert, P. and Stohl, A.: The Lagrangian particle dispersion model FLEXPART version 10.3, Geosci. Model Dev. Discuss., (January), 1–67, doi:10.5194/gmd-2018-333, 2019.

Platt, S. M., Hov, Ø., Berg, T., Breivik, K., Eckhardt, S., Hansson, H., Heintzenberg, J., Hermansen, O., Heslin-rees, D. and Holmén, K.: Atmospheric composition in the European Arctic and 30 years of the Zeppelin Observatory , Ny-Ålesund, , 3321–3369, 2022.

Quinn, P. K., Coffman, D. J., Johnson, J. E., Upchurch, L. M. and Bates, T. S.: Small fraction of marine cloud condensation nuclei made up of sea spray aerosol, Nat. Geosci., 10(9), 674–679, doi:10.1038/ngeo3003, 2017.

Rader, F., Traversi, R., Severi, M., Becagli, S., Müller, K.-J., Nakoudi, K. and Ritter, C.: Overview of Aerosol Properties in the European Arctic in Spring 2019 Based on In Situ Measurements and Lidar Data, Atmosphere (Basel)., 12(2), doi:10.3390/atmos12020271, 2021.

1048 Riddick, S. N., Dragosits, U., Blackall, T. D., Daunt, F., Wanless, S. and Sutton, M. A.: The
1049 global distribution of ammonia emissions from seabird colonies, Atmos. Environ., 55, 319–
1050 327, doi:10.1016/j.atmosenv.2012.02.052, 2012.

1051 Roldin, P., Swietlicki, E., Schurgers, G., Arneth, A., Lehtinen, K. E. J., Boy, M. and Kulmala,
1052 M.: Development and evaluation of the aerosol dynamics and gas phase chemistry model
1053 ADCHEM, Atmos. Chem. Phys., 11(12), 5867–5896, doi:10.5194/acp-11-5867-2011, 2011.

1054 Roldin, P., Ehn, M., Kurtén, T., Olenius, T., Rissanen, M. P., Sarnela, N., Elm, J., Rantala, P.,
1055 Hao, L., Hyttinen, N., Heikkinen, L., Worsnop, D. R., Pichelstorfer, L., Xavier, C., Clusius,
1056 P., Öström, E., Petäjä, T., Kulmala, M., Vehkamäki, H., Virtanen, A., Riipinen, I. and Boy,
1057 M.: The role of highly oxygenated organic molecules in the Boreal aerosol-cloud-climate
1058 system, Nat. Commun., 10(2019), 4370, doi:10.1038/s41467-019-12338-8, 2019.

1059 Rosati, B., Christiansen, S., Wollesen de Jonge, R., Roldin, P., Jensen, M. M., Wang, K.,
1060 Moosakutty, S. P., Thomsen, D., Salomonsen, C., Hyttinen, N., Elm, J., Feilberg, A., Glasius,
1061 M. and Bilde, M.: New Particle Formation and Growth from Dimethyl Sulfide Oxidation by
1062 Hydroxyl Radicals, ACS Earth Sp. Chem., acsearthspacechem.0c00333,
1063 doi:10.1021/acsearthspacechem.0c00333, 2021.

1064 Rosenfeld, D., Andreae, M. O., Asmi, A., Chin, M., de Leeuw, G., Donovan, D. P., Kahn, R.,
1065 Kinne, S., Kivekäs, N., Kulmala, M., Lau, W., Schmidt, K. S., Suni, T., Wagner, T., Wild, M.
1066 and Quaas, J.: Global observations of aerosol-cloud-precipitation-climate interactions, Rev.
1067 Geophys., 52(4), 750–808, doi:10.1002/2013RG000441, 2014.

1068 Salter, M. E., Zieger, P., Acosta Navarro, J. C., Grythe, H., Kirkeväg, A., Rosati, B., Riipinen,
1069 I. and Nilsson, E. D.: An empirically derived inorganic sea spray source function
1070 incorporating sea surface temperature, Atmos. Chem. Phys., 15(19), 11047–11066,
1071 doi:10.5194/acp-15-11047-2015, 2015.

1072 Saunders, S. M., Jenkin, M. E., Derwent, R. G. and Pilling, M. J.: Protocol for the
1073 development of the Master Chemical Mechanism, MCM v3 (Part A): Tropospheric
1074 degradation of non-aromatic volatile organic compounds, Atmos. Chem. Phys., 3(1), 161–
1075 180, doi:10.5194/acp-3-161-2003, 2003.

1076 Schemann, V. and Ebell, K.: Simulation of mixed-phase clouds with the ICON large-eddy
1077 model in the complex Arctic environment around Ny-Ålesund, Atmos. Chem. Phys., 20(1),
1078 475–485, doi:10.5194/acp-20-475-2020, 2020.

1079 Scott, C. E., Rap, A., Spracklen, D. V., Forster, P. M., Carslaw, K. S., Mann, G. W., Pringle,
1080 K. J., Kivekäs, N., Kulmala, M., Lihavainen, H. and Tunved, P.: The direct and indirect
1081 radiative effects of biogenic secondary organic aerosol, Atmos. Chem. Phys., 14(1), 447–470,
1082 doi:10.5194/acp-14-447-2014, 2014.

1083 Sofiev, M., Soares, J., Prank, M., De Leeuw, G. and Kukkonen, J.: A regional-to-global
1084 model of emission and transport of sea salt particles in the atmosphere, J. Geophys. Res.
1085 Atmos., 116(21), doi:10.1029/2010JD014713, 2011.

1086 Stock, C. A., Dunne, J. P. and John, J. G.: Global-scale carbon and energy flows through the

1087 marine planktonic food web: An analysis with a coupled physical–biological model, Prog.
1088 Oceanogr., 120, 1–28, doi:https://doi.org/10.1016/j.pocean.2013.07.001, 2014.

1089 Stohl, A., Sodemann, H., Eckhardt, S., Frank, A., Seibert, P. and Wotawa, G.: The Lagrangian
1090 particle dispersion model FLEXPART version 8 .2, 2005.

1091 Ström, J., Engvall, A. C., Delbart, F., Krejci, R. and Treffeisen, R.: On small particles in the
1092 Arctic summer boundary layer: Observations at two different heights near Ny-Ålesund,
1093 Svalbard, Tellus, Ser. B Chem. Phys. Meteorol., 61 B(2), 473–482, doi:10.1111/j.1600-
1094 0889.2008.00412.x, 2009.

1095 Traversi, R., Becagli, S., Severi, M., Caiazzo, L., Mazzola, M., Lupi, A., Fiebig, M.,
1096 Hermansen, O., Krejci, R. and Unit, A. S.: Arctic haze in a climate changing world: the 2010-
1097 2020 trend (HAZECLIC) 4, , (0000), 104–117, 2020.

1098 Tunved, P., Ström, J. and Krejci, R.: Arctic aerosol life cycle: Linking aerosol size
1099 distributions observed between 2000 and 2010 with air mass transport and precipitation at
1100 Zeppelin station, Ny-Ålesund, Svalbard, Atmos. Chem. Phys., 13(7), 3643–3660,
1101 doi:10.5194/acp-13-3643-2013, 2013.

1102 Uhlig, C., Damm, E., Peeken, I., Krumpen, T., Rabe, B., Korhonen, M. and Ludwichowski,
1103 K. U.: Sea ice and water mass influence dimethylsulfide concentrations in the central arctic
1104 ocean, Front. Earth Sci., 7(July), 1–15, doi:10.3389/feart.2019.00179, 2019.

1105 Wainwright, C. D., Pierce, J. R., Liggio, J., Strawbridge, K. B., MacDonald, A. M. and
1106 Leaitch, R. W.: The effect of model spatial resolution on Secondary Organic Aerosol
1107 predictions: A case study at Whistler, BC, Canada, Atmos. Chem. Phys., 12(22), 10911–
1108 10923, doi:10.5194/acp-12-10911-2012, 2012.

1109 Wentworth, G. R., Murphy, J. G., Croft, B., Martin, R. V., Pierce, J. R., Côté, J. S.,
1110 Courchesne, I., Tremblay, J. É., Gagnon, J., Thomas, J. L., Sharma, S., Toom-Sauntry, D.,
1111 Chivulescu, A., Levasseur, M. and Abbatt, J. P. D.: Ammonia in the summertime Arctic
1112 marine boundary layer: Sources, sinks, and implications, Atmos. Chem. Phys., 16(4), 1937–
1113 1953, doi:10.5194/acp-16-1937-2016, 2016.

1114 Wollesen de Jonge, R.: Supplement of Secondary aerosol formation from dimethyl sulfide –
1115 improved mechanis- tic understanding based on smog chamber experiments and modelling, ,
1116 9955–9976, 2021.

1117 Wollesen de Jonge, R., Elm, J., Rosati, B., Christiansen, S., Hyttinen, N., Lüdemann, D.,
1118 Bilde, M. and Roldin, P.: Secondary aerosol formation from dimethyl sulfide – improved
1119 mechanistic understanding based on smog chamber experiments and modelling, Atmos.
1120 Chem. Phys., 1–33, doi:10.5194/acp-2020-1324, 2021.

1121 Xavier, C., Rusanen, A., Zhou, P., Dean, C., Pichelstorfer, L., Roldin, P. and Boy, M.:
1122 Aerosol mass yields of selected biogenic volatile organic compounds – a theoretical study
1123 with nearly explicit gas-phase chemistry, Atmos. Chem. Phys., 19(22), 13741–13758,
1124 doi:10.5194/acp-19-13741-2019, 2019.

1125 Zheng, G., Wang, Y., Aiken, A. C., Gallo, F., Jensen, M. P., Kollias, P., Kuang, C., Luke, E.,
1126 Springston, S., Uin, J., Wood, R. and Wang, J.: Marine boundary layer aerosol in the eastern
1127 North Atlantic: Seasonal variations and key controlling processes, Atmos. Chem. Phys.,
1128 18(23), 17615–17635, doi:10.5194/acp-18-17615-2018, 2018.

1129 Ziska, F., Quack, B., Abrahamsson, K., Archer, S. D., Atlas, E., Bell, T., Butler, J. H.,
1130 Carpenter, L. J., Jones, C. E., Harris, N. R. P., Hepach, H., Heumann, K. G., Hughes, C.,
1131 Kuss, J., Krüger, K., Liss, P., Moore, R. M., Orlikowska, A., Raimund, S., Reeves, C. E.,
1132 Reifenhäuser, W., Robinson, A. D., Schall, C., Tanhua, T., Tegtmeier, S., Turner, S., Wang,
1133 L., Wallace, D., Williams, J., Yamamoto, H., Yvon-Lewis, S. and Yokouchi, Y.: Global sea-
1134 to-air flux climatology for bromoform, dibromomethane and methyl iodide, Atmos. Chem.
1135 Phys., 13(17), 8915–8934, doi:10.5194/acp-13-8915-2013, 2013.